Helsinki University of Technology
CFD-group/ Laboratory of Applied Thermodynamics

MEMO No CFD/THERMO-42-2003 DATE: 8th April 2003

TITLE

Simulation of Two Sewage Pump Geometries

AUTHOR(S)
Juhaveikko Ala-Juusela and Harri Heiska

ABSTRACT

Single-blade sewage pumps with two different geometries are simulated numerically using two flow-solver packages, a University-developed FINFLO solver and a commercial CFX-TASCFlow. Both low and high Reynolds number approaches are utilized with $k-\varepsilon$ and $k-\omega$ turbulence closures. Results are compared to the experimental data provided by Grundfos A/S.

MAIN RESULT

Pump head, efficiency and torque are obtained from the simulated flowfield. Wall-function approach under-estimates the head and the torque and over-estimates the efficiency. Low-Reynolds number simulation under-estimates all the values.

PAGES
43

KEY WORDS
FINFLO, CFX-TASCFlow, $k-\omega$ model, $k-\varepsilon$ model, water pump

APPROVED BY

Timo Siikonen 8th April 2003

Contents

Nomenclature

A	Jacobian matrix $\frac{\partial \hat{F}}{\partial U}$ in the i-direction; cell face area
C	constant
CFL	Courant number
C_p	pressure coefficient
E	total energy
F, G, H	flux vectors in the x-, y- and z-directions
Pr	Prandtl number
Q	source term vector
Re	Reynolds number
T	temperature
U	vector of conservative variables
V	velocity vector
c_p	specific heat at a constant pressure
c_v	specific heat at a constant volume
e	specific internal energy
k	turbulent kinetic energy
$\dot{m}$	mass flow
p	pressure
$\vec{q}$	heat flux
t	time
u, v, w	velocity components in the x-, y- and z-directions
u_τ	friction velocity $(= \sqrt{\tau_w/\rho})$
y^+	dimensionless distance from the wall $(= yu_\tau/\nu)$
β, β^*	artificial compressibility coefficient, model constants in the $k-\omega$ model
δ_{ij}	Kronecker's delta
ϵ	dissipation of the kinetic energy of the turbulence
θ	temperature difference $(= T - T_\infty)$
μ	dynamic viscosity
ν	kinematic viscosity
ϕ	scalar
ρ	density
τ	shear stress
ω	specific dissipation rate of turbulent kinetic energy $(= \varepsilon/(\beta^* k))$

Superscripts

T	transposition
l	left side
r	right side
w	wall value
$'$	fluctuating component

Subscripts

T	turbulent
i, j, k	$i-$, $j-$ k-component
t	tangential component
n	normal component

1 Introduction

In this study two single-blade sewage pump geometries were simulated numerically using CFX-TASCFlow flow solver package and FINFLO flow solver. The grids for CFX-TASCFlow simulations were provided by the manufacturer, Grundfos A/S.

The grid for the first geometry is aimed for a wall function approach with coarse computational cells near the walls, while the grid for the second geometry is more suitable for low-Reynolds number turbulence models. The latter is also the geometry used in measurements made by Grundfos A/S. The former grid is modified in order to make it suitable for FINFLO calculations mainly just by adding gridpoints near the solid surfaces.

The purpose of the present study is to compare the results of the two computer codes, the associated turbulence models and the required grid densities. In the following, the governing equations and turbulence modelling are firstly described. Next, the computational domain and the grid are depicted and, finally, the results of the simulation are presented and compared with the measurements.

2 Flow Solvers

2.1 FINFLO

FINFLO is an in-house Navier-Stokes flow solver capable of handling incompressible and compressible flows. The code is developed in the Helsinki University of Technology. The Reynolds-averaged thin-layer Navier-Stokes equations are solved with a finite volume method [1]. The solution methods of the FINFLO code can be found for example in [2]. There are several turbulence modelling approaches in FINFLO [1]. In this study we apply $k-\omega$ SST turbulence model which, in order to improve the near-wall behaviour of a $k-\varepsilon$ model, is a mixture of the $k-\varepsilon$ and $k-\omega$ models, known as Menter's $k-\omega$ SST model [3, 4, 5].

In these approaches turbulence is modelled as based on Boussinesq approximation in which the influence of turbulence is characterized similarly as viscosity. Turbulent kinetic energy k and its dissipation ε or specific dissipation rate $\omega = \varepsilon/\beta^* k$ are used to model the turbulent viscosity. Turbulence closures based on the solution of the k- and ε -variables can be written as

$$\nu_T = c_\mu \frac{k^2}{\epsilon} \tag{1}$$

$$\frac{\mathrm{D}k}{\mathrm{D}t} = P - \varepsilon + \frac{\partial}{\partial x_j}\left[(\nu + \frac{\nu_T}{\sigma_k})\frac{\partial k}{\partial x_j}\right] \tag{2}$$

$$\frac{\mathrm{D}\varepsilon}{\mathrm{D}t} = \frac{\varepsilon}{k}(c_{\varepsilon 1}P - c_{\varepsilon 2}f_2\varepsilon) + E + \frac{\partial}{\partial x_j}\left[(\nu + \frac{\nu_T}{\sigma_k})\frac{\partial k}{\partial x_j}\right] \tag{3}$$

The function f_2 is defind as

$$f_2 = 1 - 0.22e^{-Re_T^2/36} \tag{4}$$

and

$$E = -2\nu(\varepsilon/y_n^2)e^{-y^+/2} \tag{5}$$

where y_n is the normal distance from the wall, and the dimensionless distance y^+ is defined by

$$y^+ = y_n\frac{u_\tau}{\nu} = y_n\frac{\sqrt{\tau_w}}{\nu} \approx y_n\left[\frac{|\nabla \times \vec{V}|}{\nu}\right]_w^{1/2} \tag{6}$$

Here u_τ is a friction velocity and τ_w is shear stress on the wall, and the connection between them is $u_\tau = \sqrt{\tau_w/\rho}$. The unknown production of the turbulent kinetic energy is modelled using Boussinesq's approximation

$$\begin{aligned} P &= -\overline{u_i'' u_j''}\frac{\partial u_i}{\partial x_j} \\ &= \left[\nu_T(\frac{\partial u_i}{\partial x_j} + \frac{\partial u_j}{\partial x_i} - \frac{2}{3}\delta_{ij}\frac{\partial u_k}{\partial x_k}) - \frac{2}{3}\delta_{ij}k\right]\frac{\partial u_i}{\partial x_j} \end{aligned} \tag{7}$$

The turbulence model presented above contains empirical coefficients. Those are given by [1]

$$\begin{aligned} c_{\varepsilon 1} &= 1.44 & \sigma_k &= 1.0 \\ c_{\varepsilon 1} &= 1.92 & \sigma_\epsilon &= 1.3 \\ c_\mu &= 0.09(1 - e^{-0.0115y^+}) \end{aligned} \tag{8}$$

where the turbulence Reynolds number is defined as

$$Re_T = \frac{\rho k^2}{\mu\epsilon} \tag{9}$$

Models based on the solution of the k- and ω -variables can be written as

$$\nu_T = k/\omega \tag{10}$$

$$\frac{\mathrm{D}k}{\mathrm{D}t} = P - \beta^* k\omega + \frac{\partial}{\partial x_i}\left[(\nu + \frac{\nu_T}{\sigma_k})\frac{\partial k}{\partial x_i}\right] \tag{11}$$

$$\begin{aligned} \frac{\mathrm{D}\omega}{\mathrm{D}t} &= \omega\left(\frac{\gamma}{k}P - \beta\omega\right) \\ &+ \frac{\partial}{\partial x_i}\left[(\nu + \frac{\nu_T}{\sigma_\omega})\frac{\partial \omega}{\partial x_j}\right] \\ &+ 2\frac{1 - F_1}{\sigma_{\omega 2}\omega}\frac{\partial k}{\partial x_j}\frac{\partial \omega}{\partial x_j} \end{aligned} \tag{12}$$

The model coefficients in Eqs. (11) and (12) are obtained from

$$(\sigma_k \ \sigma_\omega \ \beta)^T = F_1 \, (\sigma_k \ \sigma_\omega \ \beta)_1^T + (1 - F_1) \, (\sigma_k \ \sigma_\omega \ \beta)_2^T \tag{13}$$

with the following values

$$\begin{array}{lll} \sigma_{k1} = 1.176 & \sigma_{\omega 1} = 2.0 & \beta_1 = 0.075 \\ \sigma_{k2} = 1.0 & \sigma_{\omega 2} = 1.168 & \beta_2 = 0.0828 \end{array}$$

Coefficients κ and β^* have constant values 0.41 and 0.09. Coefficient γ is calculated from

$$\gamma = \frac{\beta}{\beta^*} - \frac{\kappa^2}{\sigma_\omega \sqrt{\beta^*}} \tag{14}$$

In the present study the artificial compressibility approach is used to determine the pressure. The artificial compressibility can be used in order to modify a compressible flow solver for incompressible and nearly incompressible flows. The flux calculation is a simplified version of the approximate Riemann-solver utilized for compressible flows [6]. It should be noted that in this approach the artificial sound speed affects the solution, but the effect is of a second-order and is not visible as the grid is refined. The solution method is described in [7].

A third-order upwind biased discretization is used in the calculation of the convective fluxes.

2.2 CFX-TASCFlow

CFX-TASCflow is an integrated software system capable of solving diverse and complex multidimensional fluid problems. The fluid flow solver, CFX-TASCflow, provides solutions for incompressible and compressible, steady-state or transient, laminar or turbulent single-phase fluid flow in complex geometries. The solution methods of CFX-TASCflow can be found from [8].

In this study we apply $k-\varepsilon$ turbulence model for the coarse wall function grid and $k-\omega$ SST turbulence model for the refined grids. The $k-\varepsilon$ turbulence model presented in the previous section contains empirical coefficients, which are different for CFX-TASCFlow solver as the code uses wall functions.

$$\begin{array}{rclrcl} c_{\varepsilon 1} & = & 1.44 & \sigma_k & = & 1.0 \\ c_{\varepsilon 2} & = & 1.92 & \sigma_\epsilon & = & 1.3 \\ c_\mu & = & 0.09 & & & \end{array} \tag{15}$$

The wall-function approach in CFX-TASCFlow is an extension of the method of Launder and Spalding [8]. The near-wall tangential velocity is related to the wall shear-stress by means of a logarithmic relation,

$$u^+ = \frac{1}{\kappa} \ln(y^+) \tag{16}$$

where

$$u^+ = \frac{V_t}{u_\tau} \tag{17}$$

$$y^+ = \frac{\rho y_n u_\tau}{\mu} \tag{18}$$

$$u_\tau = \left(\frac{\tau_w}{\rho}\right)^1 /2 \tag{19}$$

Above y^+ is the non-dimensional wall distance, τ_w is the wall shear-stress, V_t is the known velocity tangential to the wall, y_n is a distance from the wall and κ is the von Karman constant. In the logarithmic region, an alternative velocity scale u^* can be used instead of u^+ in order to avoid a singularity at separation points:

$$u^* = c_\mu^{1/4}\sqrt{k} \tag{20}$$

Based on this definition, the equation for the wall shear-stress is obtained:

$$\tau_w = \tau_{visc}\frac{y^*}{u^+} \tag{21}$$

where

$$\tau_{visc} = \mu V_t / y_n \tag{22}$$

$$y^* = \rho u^* y_n / \mu \tag{23}$$

$$u^+ = \frac{1}{\kappa}\ln(y^*) \tag{24}$$

For this type of scalable wall-function the y^+ value should not be below $y^+ = 11$ [8].

The discretization scheme used is linear profile skew that is according to the manual truly second-order accurate.

3 Computational Domains and Grids

Two different geometries were used, that differ slightly from each other. The first one was simulated using both codes, while the latter, that is the same geometry that is used in measurements, only with Tascflow. The first geometry is from now on referred as geometry 2.1 and the latter as geometry 2.2. Both geometries are shown in Fig. 1 as well as an overlap figure of the two geometries. This shows the difference between these two models. The design point mass flow is 25 kg/s for geometry 2.1 and 33 kg/s for geometry 2.2. The rotational speed is 1450 RPM corresponding to an angular velocity of 24.17 1/s.

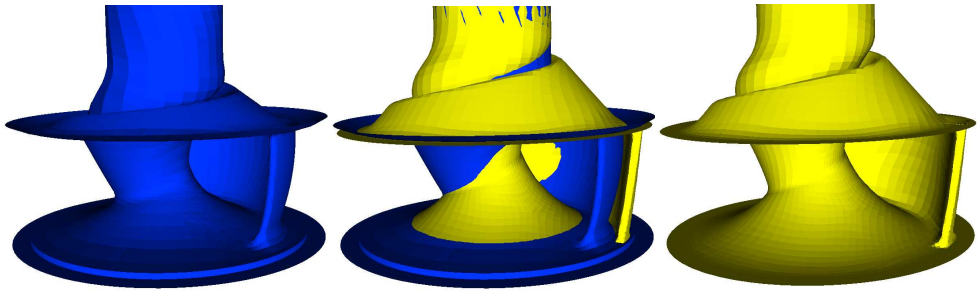

Fig. 1: From left to right: Geometry 2.1, overlap of the geometries and geometry 2.2.

3.1 Geometry 2.1

3.1.1 Wall Function Grid

The computational grid is of a structured type suitable for simulations with wall functions. The grid is provided by the manufacturer, Grundfos A/S. The grid has 18 blocks. In the impeller part there are 11 blocks and seven in the volute part. The computational model consists of two separed parts: A single-blade impeller and a volute. The grid lines at the interface between the parts are not continuous. The grid structure and the surface grid are shown in Fig. 2. The dimensions of the grid are given in Table 1.

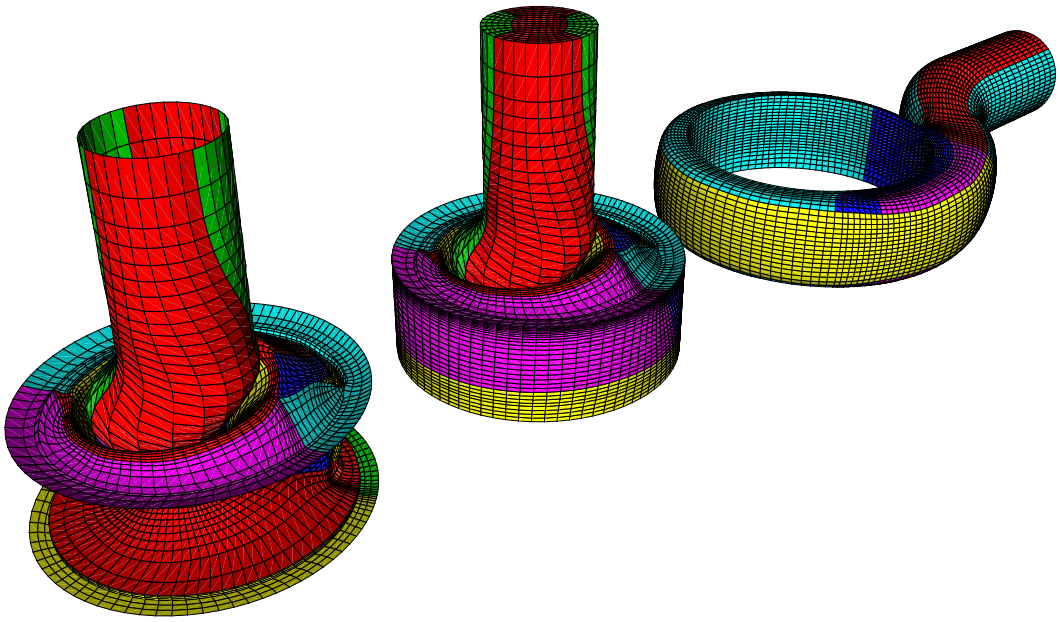

Fig. 2: Computational grid for the wall-function approach. From left to right: Impeller surface, impeller grid and volute grid.

Table. 1: Dimensions of the wall-function grid.

Explanation	Block	i	j	k	$\sum$
Impeller	1	24	8	18	3 456
Impeller	2	88	5	8	3 520
Impeller	3	16	8	50	6 400
Impeller	4	10	105	16	16 800
Impeller	5	36	21	8	6 048
Impeller	6	64	8	5	2 560
Impeller	7	221	5	5	5 750
Impeller	8	24	3	56	4 032
Impeller	9	32	8	5	1 280
Impeller	10	44	3	8	1 056
Impeller	11	48	5	16	3 840
Volute	12	16	22	36	12 672
Volute	13	36	3	16	1 728
Volute	14	36	16	3	1 728
Volute	15	8	48	22	8 448
Volute	16	16	3	104	4 992
Volute	17	24	22	8	4 224
Volute	18	8	64	22	11 264
				Total	99 798

3.1.2 Clustered Grid

This grid is modified from the wall-function grid by adding gridpoints near the walls, so that a low-Reynolds number turbulence model can be used. Unfortunately grid dimensions could not be changed in all blocks so that multi-grid method could be used to accelerate the convergence. The grid has 11 blocks of which seven are for impeller part and four for the volute. The grid structure and the surface grid are shown in Fig. 3. The dimensions of the grid are given in Table 2.

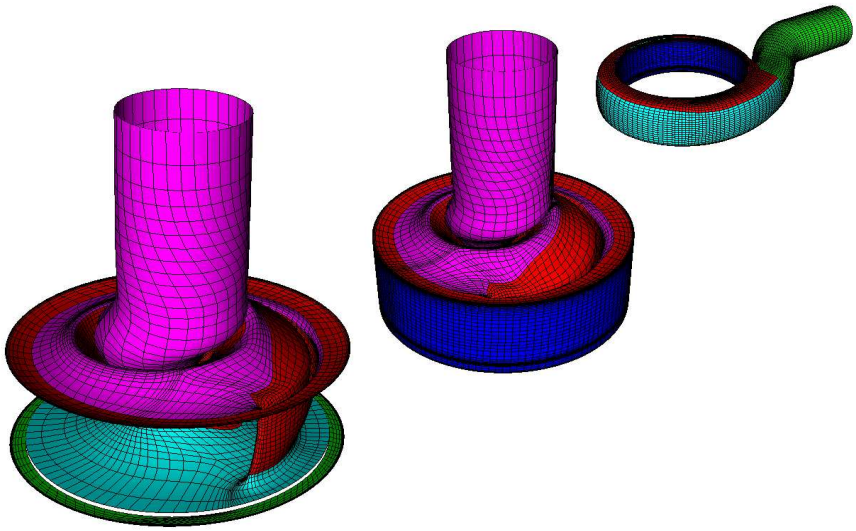

Fig. 3: Computational grid for the low-Reynolds number model. From left to right: Impeller surface, impeller grid and volute grid.

Table. 2: Dimensions of the refined grid for geometry 2.1.

Explanation	Block	i	j	k	$\sum$
Impeller	1	24	16	32	12 288
Impeller	2	56	8	8	3 584
Impeller	3	48	8	29	11 136
Impeller	4	16	16	174	44 544
Impeller	5	48	5	149	35 760
Impeller	6	64	8	100	51 200
Volute	7	64	8	100	51 200
Volute	8	48	8	136	52 224
Volute	9	16	16	104	26 624
Volute	10	16	16	36	9 216
Volute	11	16	64	36	36 864
				Total	334 640

3.2 Geometry 2.2

This grid is clustered near the walls, so the low-Reynolds number turbulence models can be used. The geometry is different from the previous one in the blade area and there is no step at the bottom of the impeller wheel. In the volute, the upper part comes down to the outer surface of the impeller wheel. Also the inlet and the outlet ducts are longer. Otherwise the volutes are quite similar. The grid has 19 blocks of which 10 are in the impeller part and nine in the volute. The grid structure and the surface grid are shown in Fig. 4. The dimensions of the grid are available in Table 3.

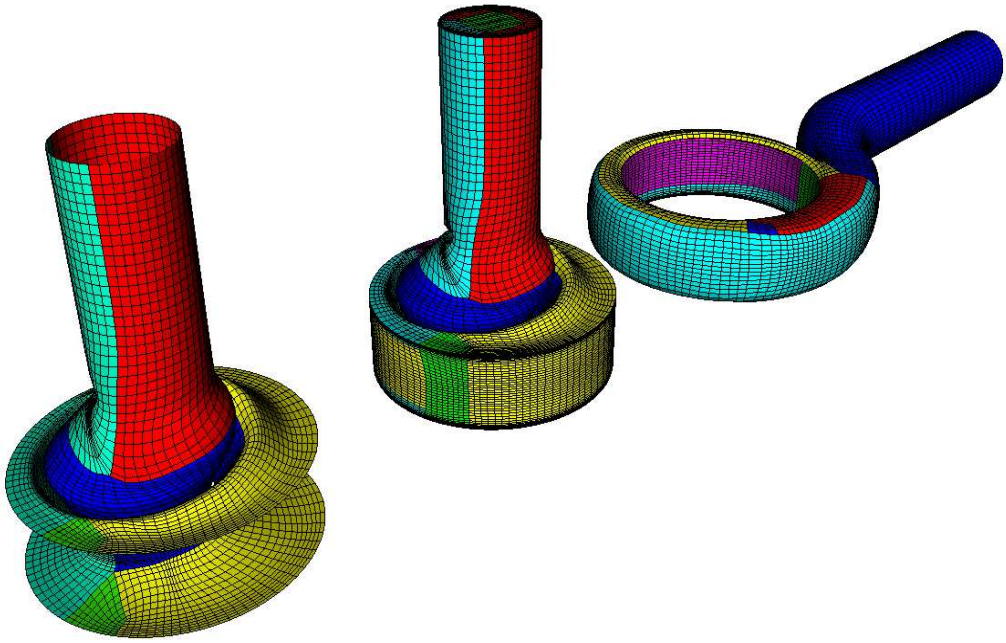

Fig. 4: The computational grid for geometry 2.2. From left to right: Impeller surface, impeller grid and volute grid.

4 Boundary Conditions

The inlet flow is given as a bulk mass flow for CFX-Tascflow simulations and a fully-developed duct flow is used in FINFLO simulations. The intencity of turbulence is 5 % and for a non-dimensional turbulent viscosity μ_T/μ a value of 10 is used in CFX-Tascflow simulations. The inlet pressure is extrapolated from the computational domain. The outlet pressure is given and velocities are extrapolated.

Table. 3: Dimensions of the grid for the geometry 2.2.

Explanation	Block	i	j	k	$\sum$
Impeller	1	36	16	15	8 640
Impeller	2	36	15	32	17 280
Impeller	3	50	50	16	40 000
Impeller	4	8	50	8	3 200
Impeller	5	15	20	126	37 800
Impeller	6	8	20	48	7 680
Impeller	7	10	35	34	11 900
Impeller	8	10	56	15	8 400
Impeller	9	32	30	15	14 400
Impeller	10	10	32	10	3 200
Volute	11	46	54	17	42 228
Volute	12	46	11	16	8 096
Volute	13	6	78	11	5 148
Volute	14	97	19	17	31 331
Volute	15	9	24	11	2 376
Volute	16	3	32	39	3 744
Volute	17	3	3	33	297
Volute	18	24	22	3	1 584
Volute	19	3	22	70	4 620
				Total	251 924

5 Results

5.1 Geometry 2.1

The geometry was simulated using two different grids, a coarser grid for the wall function turbulence model and a refined grid for the low-Reynolds number turbulence models. In FINFLO the $k-\omega$ SST turbulence model with a rotational correction was utilized. CFX-TASCflow simulations were made using the $k-\varepsilon$ model with wall functions, i.e. with the coarser grid.

5.1.1 Tascflow Simulations

The calculations were carried out in two phases. First-order upwind discretization scheme was used at the start for the first 100 cycles and the calculation was continued with the skewed second-order upwind discretization. The second part was calculated 300 cycles, in which time converged results were achieved. Actually the convergence does not need all the 300 cycles, but as the simulation was let to run over night, there was no use to calculate lesser cycles. The calculation time was about four hours for the first phase and 11 hours for the second phase in all cases. Silicon Graphics Origin 2000 with one MIPS R10000 250 MHz processor was used in all calculations.

The time step, that in the steady state simulation provides relaxation to solution procedure, is 0.01 s. Calculation times are shown in Table 4. Examples of the convergence histories of the last 300 cycles are depicted in Figs. 5 and 6. The simulation time in the figures is the time step times the number of cycles.

Table. 4: Simulation parametres

Mass flow	CPU time 2nd-order. dis.	CPU time total	CPU time /cycle/cell
8.33 kg/s	10 h 46 m	14 h 23 m	1.297 ms
16.67 kg/s	11 h 8 m	14 h 48 m	1.335 ms
33.33 kg/s	10 h 49 m	14 h 39 m	1.322 ms

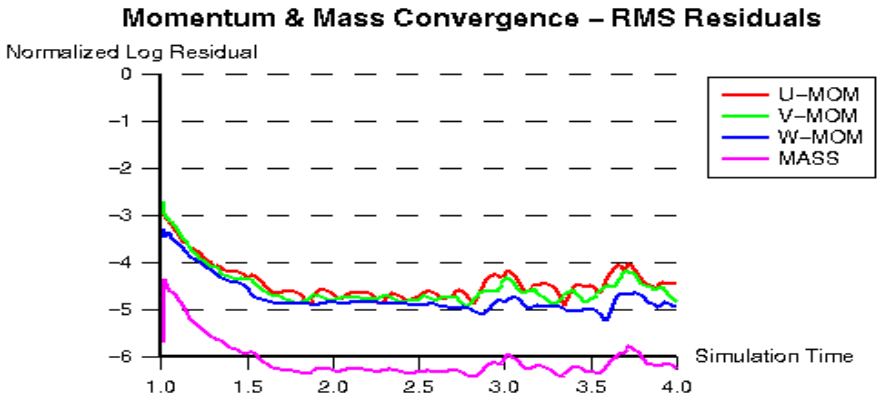

Fig. 5: Convergence histories of the momentum and mass residuals at massflow of 33.3 kg/s. Last 300 cycles of the calculation.

A static head is calculated from

$$H_{stat} = \frac{p_2 - p_1}{\rho g} \tag{25}$$

where p_1 is the inlet pressure, p_2 the outlet pressure; ρ the density, and g the acceleration due to gravity. The efficiency is obtained from

$$\eta = \Delta E / T\omega \tag{26}$$

where ΔE is the difference between the mechanical flux at the inlet and the outlet and $T\omega$ is the required axial power. The static head, efficiency and axial power needed are presented in Table 5.

It can be seen that the first-order results differ significantly from those calculated by the second-order discretization. This indicates that for reliable simulations it must not be used. In TASCFlow there are, unfortunately, many

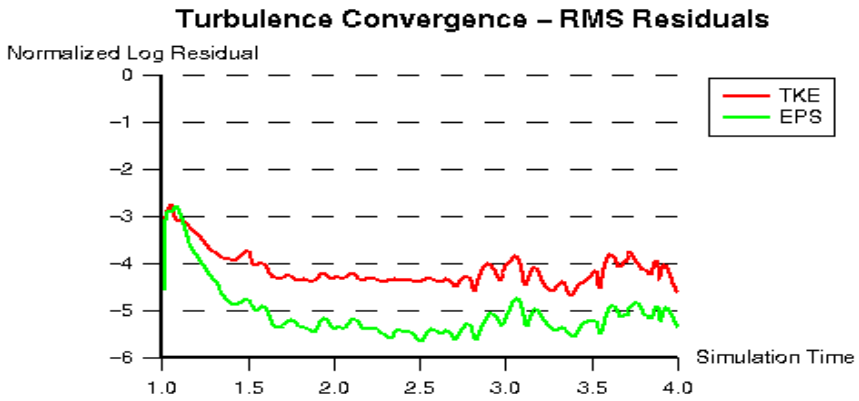

Fig. 6: Convergence histories of the residuals of the turbulence variables at massflow of 33.3 kg/s. Last 300 cycles of the calculation.

Table. 5: Pump performance.

Mass flow	Static head	Efficiency	Axial power
2nd-order upwind			
8.33 kg/s	11.7 m	60.1 %	1624 W
16.67 kg/s	9.7 m	84.5 %	1896 W
33.33 kg/s	5.1 m	72.9 %	2292 W
1st-order upwind			
8.33 kg/s	12.0 m	52.89 %	1899.7 W
33.33 kg/s	5.5 m	72.0 %	2497 W
Measurements			
8.33 kg/s	14.1 m	47.4 %	2400 W
16.67 kg/s	11.6 m	66.3%	2800 W
33.33 kg/s	7.4 m	67.7 %	3500 W

options which share the first-order accuracy. It should be noted that from the present results it is not clear whether the grid density is satisfactory even for the second-order method.

Distributions at the mass flow 33.3 kg/s on the plane at a distance of 45 mm from the bottom of the impeller for velocity, turbulent viscosity, turbulent kinetic energy, dissipation and pressure are shown in Figs. 15 - 17 of Appedix A. In Fig. 17 there is also a pressure distribution at the planes crossing the impeller. Streamlines coloured by the velocity distribution and velocity vectors at the measurement point with a pressure distribution on the solid surfaces are shown in Fig. 18. Velocity distributions and distributions of turbulent viscosity at the beginning and at the end of the inlet duct are shown in Figs. 19 - 20. Velocity distributions at the measurement stations given in Fig. 7 are available in Figs. 21 and 22.

Similar figures at the mass flow of 16.7 kg/s are shown in Figs. 23 - 30 of Appendix A and at the mass flow of 8.3 kg/s the results are given in Figs. 31 - 38 of Appendix A.

The velocity in the figures is relative to the rotation in the impeller blocks. In the volute blocks the velocity is in the inertial coordinate system. Velocity distributions are quite similar with different mass flows. The difference is in the middle of the impeller, where the velocity is smaller at the lowest mass flow. In the volute part a high-speed area is in a different place, so that when the mass flow is larger, the high-speed area is near the outlet duct. In the beginning of the outlet duct there is a low-speed area, which is a consequence of a backflow to the volute from the outlet duct.

Distributions of the turbulent viscosity differ more significantly, as at the mass flow of 33.3 kg/s the turbulent viscosity has its largest value in the outlet duct and it is larger in the volute area than in the impeller. At the lower mass flows turbulent viscosity is smaller in most of the volute area than in the impeller, largest values are near the beginning of the outlet duct. In the impeller and the inlet duct area the turbulent viscosity behaves very differently at different mass flows. As the value is low at the mass flow of 33.3 kg/s, it turns to very high at the lowest mass flow. This probably originates from the rotation in the inlet duct at lower mass flows. Distribution of the turbulent kinetic energy is quite similar in both low-mass flow cases while at the largest mass flow the high-turbulence area is larger but there is no peak value near the volute lip. The area of high dissipation grows as the mass flow decreases.

Pressure distributions show that pressure is higher in the volute than in the outlet at the largest mass flow. This phenomena does not appear at the lower mass flows.

Streamlines, i.e. paths of massless particles, are started on a plane near the inlet. At the largest mass flow streamlines go straight through the inlet duct, while at the lower mass flows they are rotating with the surface. The prerotation explains higher turbulent viscosity values in this area as the $k-\varepsilon$ turbulence model tends to generate turbulent viscosity in the middle of the vortex. It should be noted that this phenomena is typical for many turbulence models, but it is not necessary true. Streamlines also indicate that the flow from the outlet duct back to the volute is coming deeper from the duct as the mass flow decreases. At no mass flow value the flow is rotating in the outlet duct.

Velocity distributions are flat in the beginning of the inlet duct as the flow is given as a bulk flow. At the end of the duct the the flow is fastest at one side of the duct and on the other side it is even negative at the lowest mass flow. Turbulent viscosity is higher near the walls except at the lowest mass flow, in which the turbulent viscosity is on a much higher level than at the other mass flows. This is probably due to a more rotating flow in inlet duct.

Velocity distributions are quite near the measurements at measurement point one. The values at measurement point two are not well predicted. One must keep in mind, that this geometry is not exactly the same that was used

in the measurements which explains at least part of the differences.

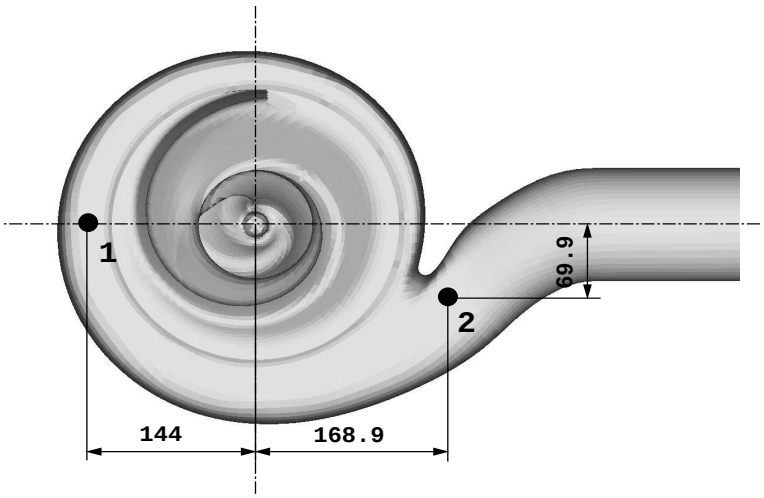

Fig. 7: Locations of the measurement points.

5.1.2 FINFLO Simulations

The $k-\omega$ SST turbulence model was utilized in these simulations. The simulations converged extremely slowly, because the multi-grid acceleration could not be used in all blocks. The computation times were between 10 to 25 days using Silicon Graphics Origin 2000 with four MIPS R10000 250 MHz processors. These figures can be significantly reduced with a more suitable grid-point distribution, i.e. the number of grid points in each coordinate direction should be powers of two. Pressure and rolling moment converged quite fast as compared to mass and momentum residuals or turbulence quantities. Examples of the convergence history of the calculations are presented in Figs. 8 - 10.

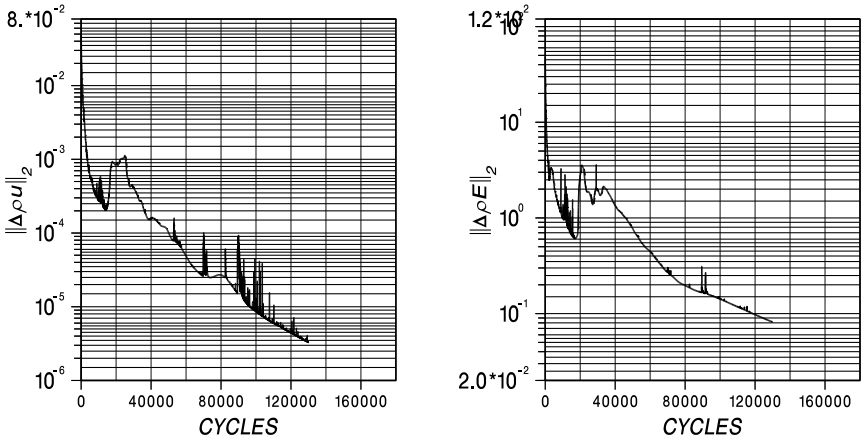

Fig. 8: Convergence history of the $||L||_2$-norm of the x-momentum residual (left) and the $||L||_2$-norm of the energy residual (right).

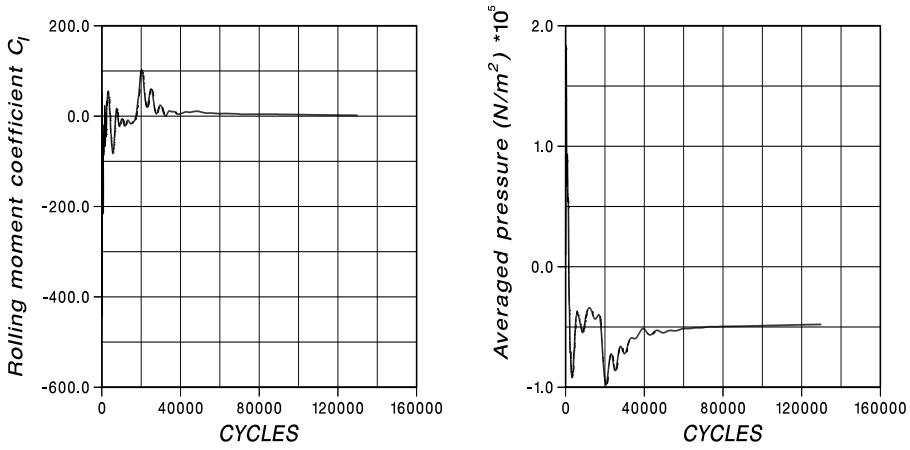

Fig. 9: Convergence history of the rolling moment (left) and the volume averaged pressure difference (right).

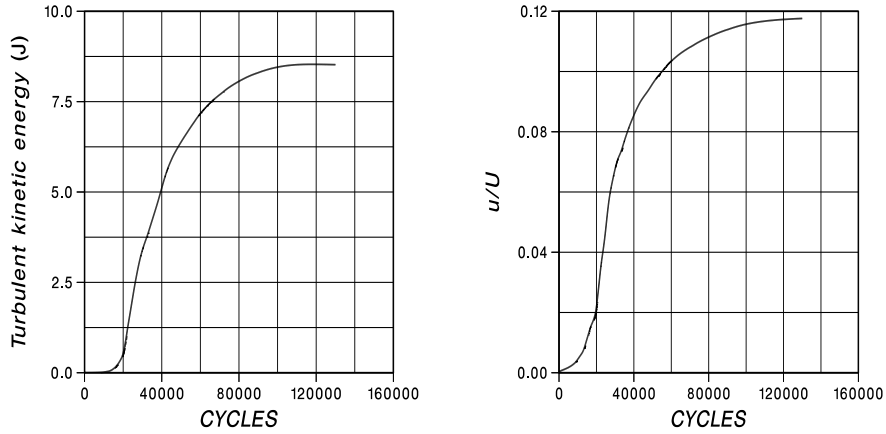

Fig. 10: Convergence history of the turbulent kinetic energy (left) and the turbulent fluctuation velocity over main velocity (right).

The static head, efficiency and axial power needed are presented in Table 6 and in Fig. 11. Static head is 20 - 40 % larger than the measured one, except at the lowest mass flow calculated. Efficiency is at its peak value at the mass flow of 20 kg/s as in the measurements, but the difference to the measured values is about 5 percentage units higher at the mass flows higher than 15 kg/s. The power need oscillates 10 % on both sides of the measured data. The CFX-TASCflow results utilizing the second-order discretization underestimate the head and the power need and the efficiency is too high. The simulation results given by Grundfos A/S (Tascflow High-Re Turb. model in the figures) are near the measurements, but similar results were also achieved when the case was accidentally calculated with the impeller surface moving at a double speed. In that case the first-order discretization was utilized.

The distributions of velocity and turbulent viscosity at 45 mm from the bottom of the impeller are shown in Fig. 39 and at the beginning and at

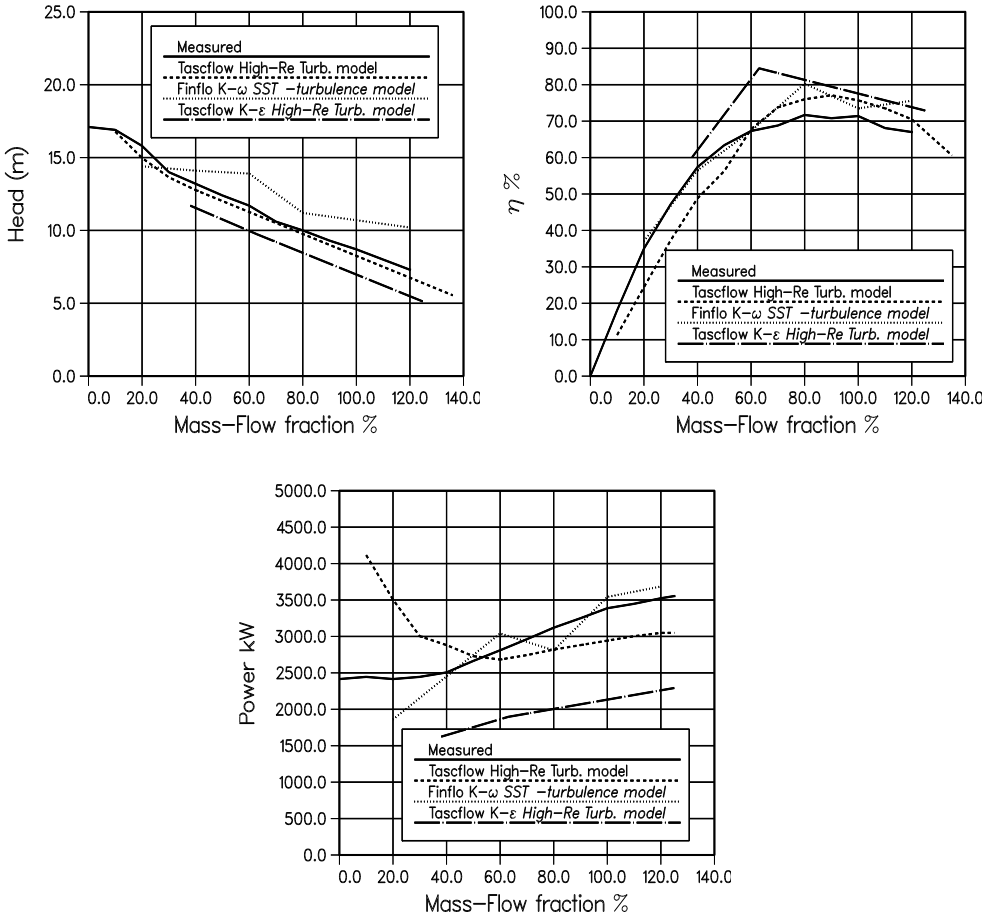

Fig. 11: Pump performancefor geometry 2.1.

the end of the inlet duct in Figs. 40 - 41. Velocity distributions from the measurement stations given in Fig. 7 are depicted in Figs. 42 and 43.

Similar figures at the mass flow of 15 kg/s are shown in Figs. 44 - 30 of Appendix B and at the mass flow of 10 kg/s the results are given in Figs. 49 - 38 of Appendix B.

The velocity is in an inertial coordinate system in all parts of the grids. A low-speed area is near the start of the outlet duct as with CFX-TASCFlow simulations but in this case it is also volute side of the lip. Turbulent viscosity is very high in the volute area also at the largest mass flow while with CFX-TASCFlow it is high only in outlet duct.

The inlet duct velocity distribution is at the start of the duct different from the CFX-TASCFlow simulations as the fully developed pipe flow is used in the inlet boundary. At the end of the duct the flow is slower on one side of the duct. The shape of the low-speed area is a bit different from the CFX-TASCFlow simulations.

Interestingly the turbulent viscosity is in all cases lower at the beginning of the duct than at the end. This is especially true at the highest mass flow.

At measurement point one the velocity levels are close to the measured ones at the mass flow of 30 kg/s. The shape especially in the radial velocity is not so close to the measurements, the shape is similar to the CFX-TASCFlow results. Neither code succeeded in prediction of the double-peaked profile. At mass flows 10 and 15 kg/s the tangential velocity level is up to 40 % lower than the measured values and also lower than the corresponding CFX-TASCFlow result, but the radial velocity is very near the measurements.

At measurement point two the velocity prediction is not so good. Only at the 30 kg/s mass flow both radial and tangential velocities resemble the measured values.

Table. 6: Pump performance.

Mass flow	Static head	Efficiency	Axial power
FINFLO simulations			
5 kg/s	14.4 m	37.0 %	1860 W
10 kg/s	14.1 m	56.5 %	2452 W
15 kg/s	13.9 m	67.3 %	3041 W
20 kg/s	11.2 m	80.3 %	2809 W
25 kg/s	10.7 m	73.5 %	3542 W
30 kg/s	10.2 m	75.6 %	3685 W
Measurements			
5 kg/s	15.8 m	24.4 %	2415 W
10 kg/s	13.2 m	48.8 %	2506 W
15 kg/s	11.7 m	67.8 %	2810 W
20 kg/s	10.0 m	76.0 %	3120 W
25 kg/s	8.7 m	75.7 %	3387 W
30 kg/s	7.3 m	70.5 %	3524 W

5.2 Geometry 2.2

5.2.1 Tascflow Simulations

The $k-\omega$ SST turbulence model was utilized in these simulations with a dense grid. Also these calculations were carried out in two phases. First-order upwind discretization was used at the start for 100 cycles and the calculation was continued with the skewed second-order upwind discretization. The second part was calculated for 100 cycles at a design point and 200 cycles at 50 % of the design point. The time step, that in the steady state simulation provides relaxation to solution procedure, is 0.01. Calculation times are shown in Table 7. Examples of the convergence histories of the last 100 cycles are shown in Figs. 12 and 13. The simulation time in the figures is the time step times the number of cycles. The position of the impeller is different from the calculation with the first geometry (2.1). This may have some influence on the

results. Most accurate quasi-steady results could be obtained by averaging the simulation results from several blade positions.

Table. 7: Simulation parametres

Mass flow	CPU time 2nd-order. dis.	CPU time total	CPU time /cycle/cell
16.67 kg/s	15 h 23 m	23 h 39 m	1.126 ms
33.33 kg/s	7 h 42 m	14 h 49 m	1.059 ms

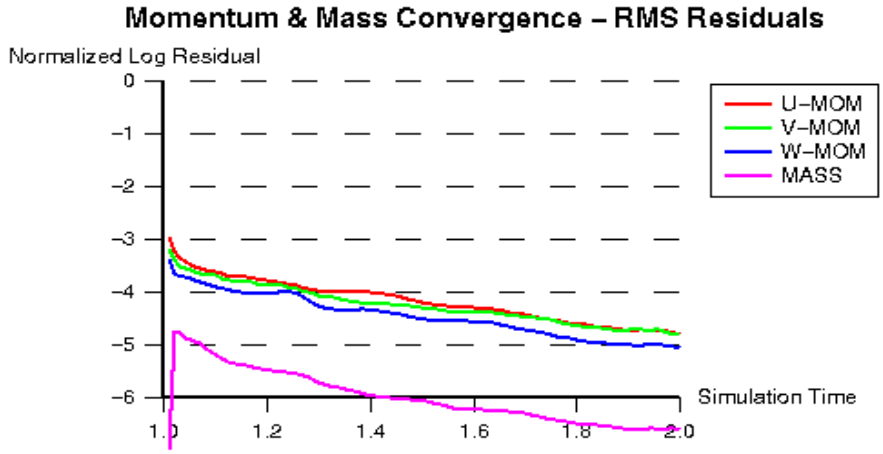

Fig. 12: Convergence histories of the momentum and mass residuals at the mass flow of 33.3 kg/s. Last 100 cycles of the calculation.

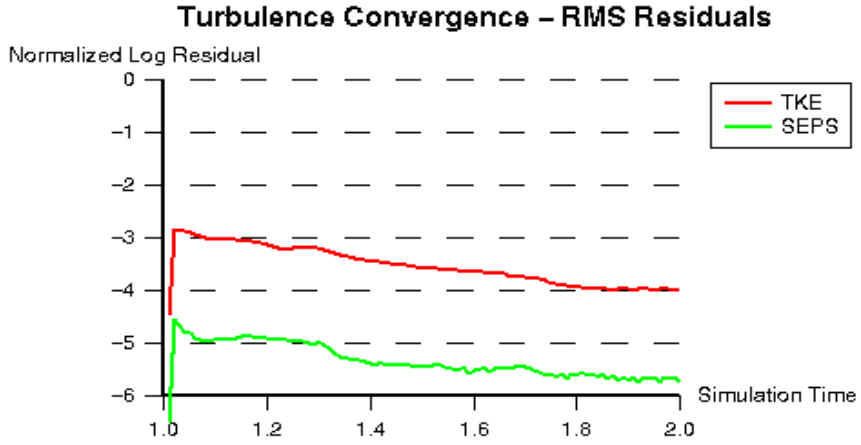

Fig. 13: Convergence histories of the residuals of the turbulence variables at a mass flow of 33.3 kg/s. Last 100 cycles of the calculation.

The static head, efficiency and axial power needed are presented in Table 8. The predicted power is much larger than with geometry 2.1 and also higher than in the measurements.

Table. 8: Pump performance for geometry 2.2.

Mass flow	Static head	Efficiency	Axial power
2nd-order upwind			
8.33 kg/s	n. a.	n. a.	n. a.
16.67 kg/s	12.80 m	57.29 %	3662 W
33.33 kg/s	8.39 m	65.44 %	4192 W
Measurements			
8.33 kg/s	18.9 m	41.7%	3640 W
16.67 kg/s	16.4 m	65.4%	4375 W
33.33 kg/s	12.4 m	71.1 %	5675 W

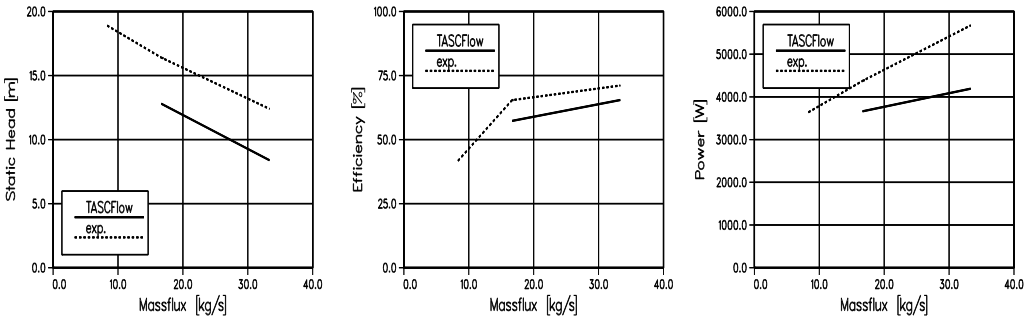

Fig. 14: Pump performance for geometry 2.2.

Distributions at the design point mass flow 33.3 kg/s at the plane 45 mm from the bottom of the impeller are shown in Figs. 54 - 56 of Appendix C for velocity, turbulent viscosity, turbulent kinetic energy, dissipation and pressure. In Fig. 56 there is also a pressure distribution on the impeller surface. Streamlines coloured by the velocity distribution and velocity vectors at the measurement point with pressure distribution on the volute and impeller surfaces are shown in Fig. 57. The low-speed vortex area depicted by the streamlines can be seen in Fig. 58. Velocity distributions from the measurement stations given in Fig. 7 are available in Figs. 59 and 60.

Similar figures at the mass flow of 16.7 kg/s (50 % of the design point mass flow) are shown in Figs. 23 - 67 of Appendix C.

The velocity distributions behave similarly as with the first geometry. The low-speed area in the beginning of the outlet duct is more visible than with the first geometry at the low mass flow value. The turbulent viscosity gets higher values in the volute part at the design point and also in the impeller part at

the lower mass flow. As with the first geometry, the pressure in the volute is at its highest value on the opposite side of the outlet duct. At the lower mass flow the pressure is also higher in that region than in the rest of the volute.

From the streamline figures it can be seen, that the flow is not rotating in the outlet duct at the design point, but at the lower mass flow that is the case. Also the streamlines show that at the design point mass flow the low-speed area in the beginning of the outlet duct consists merely of forward going vortices, at the lower mass flow there is a clear backflow.

Velocity distributions in measurement point one show that the tangential velocity is near the measured level in the lower half of the measured sweep, but in the upper half the tangential velocities are clearly lower than the measured values. Radial velocities differ significantly from the measured data. In measurement point two the tangential velocities differ significantly from the measurements like in the other simulations. Radial velocities are near the experimental values close to the upper part of the outlet duct. In the lower section of the duct the radial velocities are lower, at the low mass flow even the direction is different. At the design point velocity prediction is tolerable, but the accuracy could be better. At the lower mass flow the prediction is not satisfactory.

6 Discussion

Two sewage pump geometries were simulated numerically with multiple mass flow rates. The first geometry with a design point of 25 kg/s was simulated using two different flow solvers FINFLO and CFX-TASCFlow, while the second one with a design point of 33.3 kg/s only with CFX-TASCFlow.

The results of the simulations are not very promising, the head, the efficiency and the power need are all several percentages off the measured values. The position of the impeller may affect to the pump performance on a quasi-static simulation, therefore, the simulations should be done at least in one additional position. At the design point the predicted velocity is on a correct level at the measurement point, but the shape of the distribution is not close the measured one. At the lower mass flows the shapes and even the velocity levels differ from the measurements.

First-order discretization is inaccurate and it must not be used. Second-order discretization gives more accurate results, but the grid density is probably inadequate in present case. The inlet-flow is given as a bulk flow in TASCFlow simulations. This may cause troubles for convergence and also affect the results. Fully-developed pipe flow should be tested as an inlet flow boundary conditions.

FINFLO simulations for geometry 2.1 overestimate the head as the CFX-TASCFlow underestimates it. The power is oscillating around the measurements data for mass flows over 40% of design point. All simulated results overestimate the efficiency near the design point. A poor convergence may

induce anomalies seen in the FINFLO results. Despite of the huge amounts of computational cycles, it is not clear that all of the computations are fully converged. The code is designed to work with multi-grid acceleration and in this case it could not be used leading to a highly inefficient computation. The velocity distributions are about as accurate as CFX-TASCFlow results, on some cases even more accurate. The measured distributions are for a different impeller geometry than the simulated one. Also the quasi-static simulation can overestimate such a time-depended phenomenon as a backflow, which effects the distributions in measurement point two.

In a future a denser grid will be utilized at least for FINFLO. FINFLO results for the geometry 2.2 will be published as a separate report.

References

[1] *FINFLO User Manual version 2.2*, 1997.

[2] Ala-Juusela, J., "Simulations of a Water Pump Impeller, CFD/TERMO-40-2001, unpublished," Helsinki University of Technology, Laboratory of Applied Thermodynamics, September 2002.

[3] Menter, F., "Zonal two equation $k-\omega$ turbulence models for aerodynamic flows," in *24th AIAA Fluid Dynamics Conference*, AIAA, 1993. AIAA Paper 93–2906.

[4] Menter, F., "Two-equation eddy-viscosity turbulence models for engineering applications," *AIAA Journal*, Vol. 32, No. 8, 1994, pp. 1598–1605.

[5] Hellsten, A. and Laine, S., "Extension of the $k-\omega$ Shear-Stress Transport Turbulence Model for Rough-Wall Flows," *AIAA Journal*, Vol. 36, No. 9, 1998, pp. 1728–1729.

[6] Siikonen, T., "An application of Roe's flux-difference splitting for the $k-\epsilon$ turbulence model," *International Journal for Numerical Methods in Fluids*, Vol. 21, No. 11, 1995, pp. 1017–1039.

[7] Rahman, M., Rautaheimo, P., and Siikonen, T., "Numerical Study of Turbulent Heat Transfer from a Confined Impinging Jet Using a Pseudo-compressibility Method," in *Proceedings of the 2nd International Symposium on Turbulence, Heat and Mass Transfer*, (Delft), pp. 511–520, June 1997.

[8] AEA Technology Engineering Software, 554 Parkside Drive, Waterloo, Ontario, Canada N2L 5Z4, *CFX-TASCflow Computational Fluid Dynamics Software, Theory Documentation*, 2001.

A Distributions of the Tascflow Simulations of the Wall Function Grid

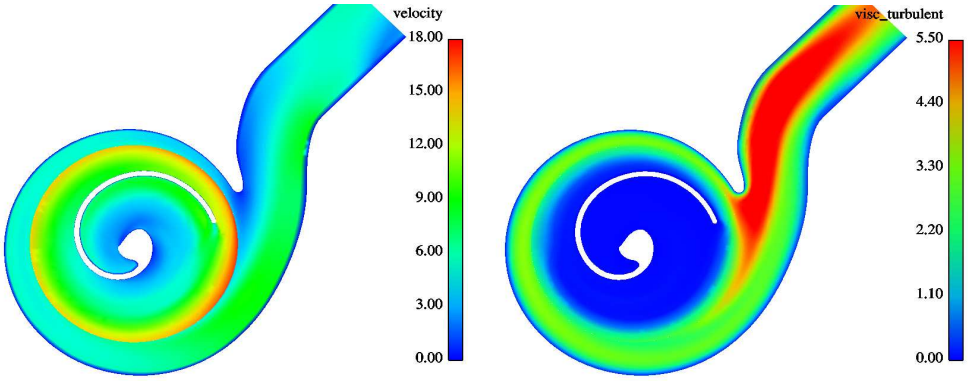

Fig. 15: Velocity distribution at plane 45 mm from the bottom of the impeller (left) and a distribution of the turbulent viscosity at same plane (right). The mass flow is 33.3 kg/s.

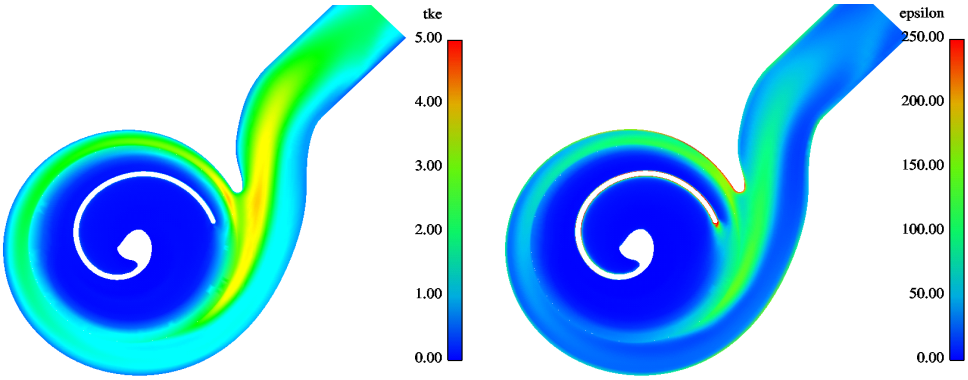

Fig. 16: Distribution of the turbulent kinetic energy (left) and dissipation (right). The plane is the same as in Fig. 15. The mass flow is 33.3 kg/s.

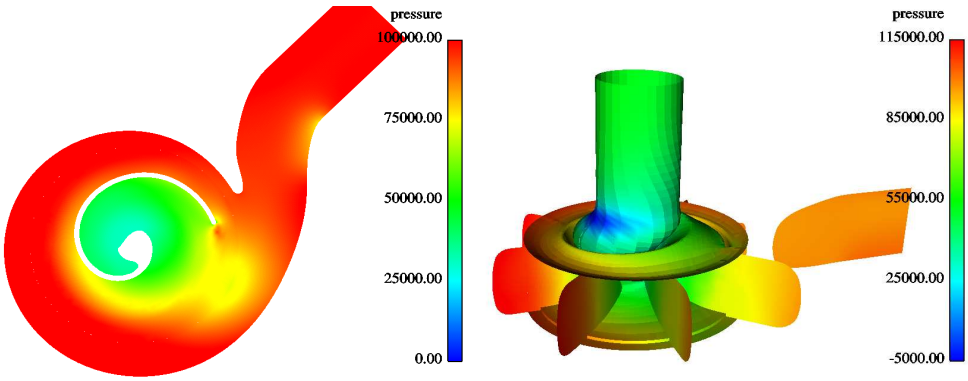

Fig. 17: Pressure distribution at plane 45 mm from the bottom of the impeller (left) and pressure distribution at planes crossing the impeller (right). The mass flow is 33.3 kg/s.

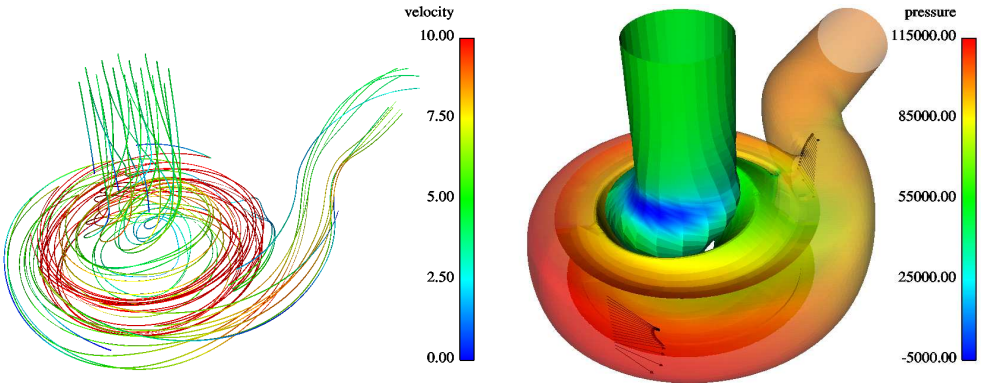

Fig. 18: Streamlines coloured by velocity distribution (left) and velocity vectors at measurement point and pressure distribution at surfaces (right). The mass flow is 33.3 kg/s.

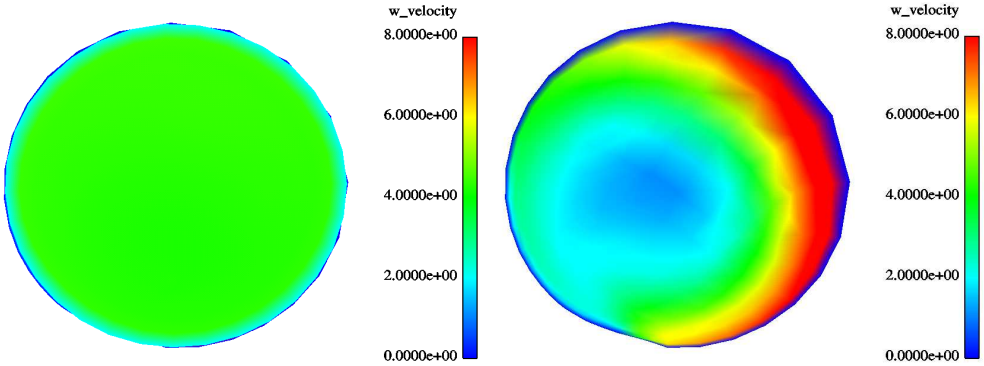

Fig. 19: Velocity distribution at the beginning (left) and at the end (right) of the inlet duct. The mass flow is 33.3 kg/s.

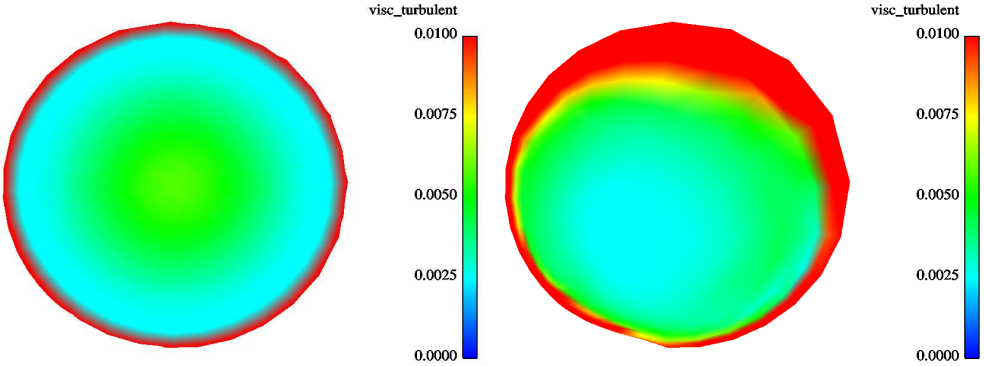

Fig. 20: Distribution of the turbulent viscosity at the beginning (left) and at the end (right) of the inlet duct. The mass flow is 33.3 kg/s.

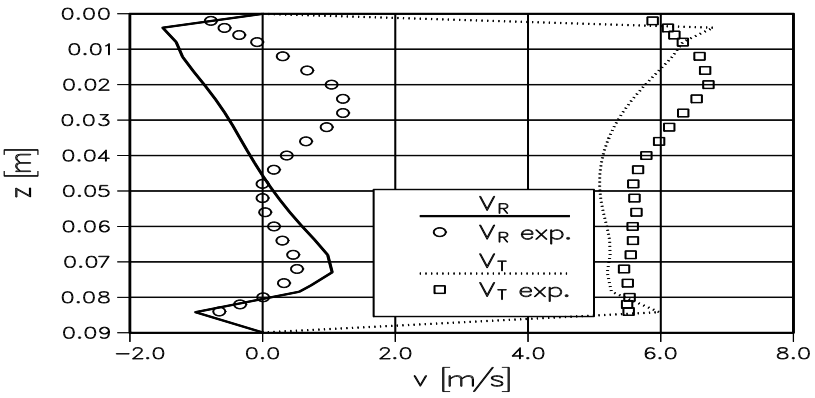

Fig. 21: Velocity distributions at measurement point 1. The mass flow is 33.3 kg/s.

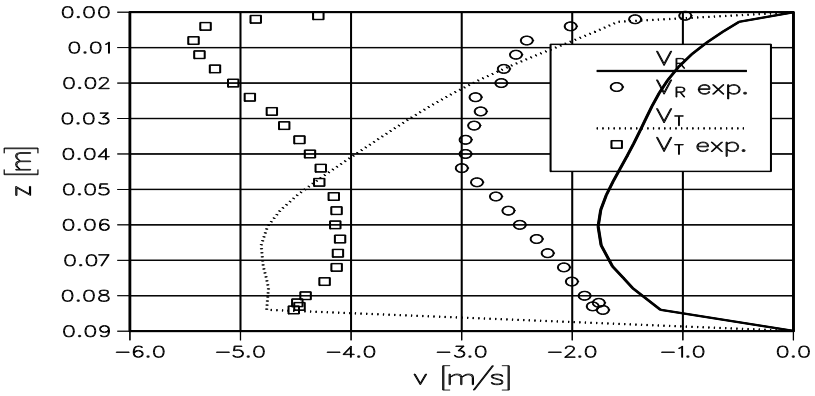

Fig. 22: Velocity distributions at measurement point 2. The mass flow is 33.3 kg/s.

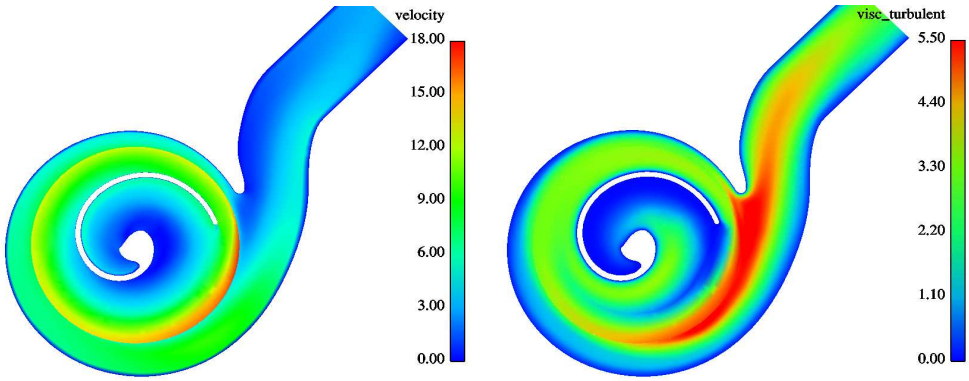

Fig. 23: Velocity distribution at plane 45 mm from the bottom of the impeller (left) and a distribution of the turbulent viscosity at same plane (right). The mass flow is 16.7 kg/s.

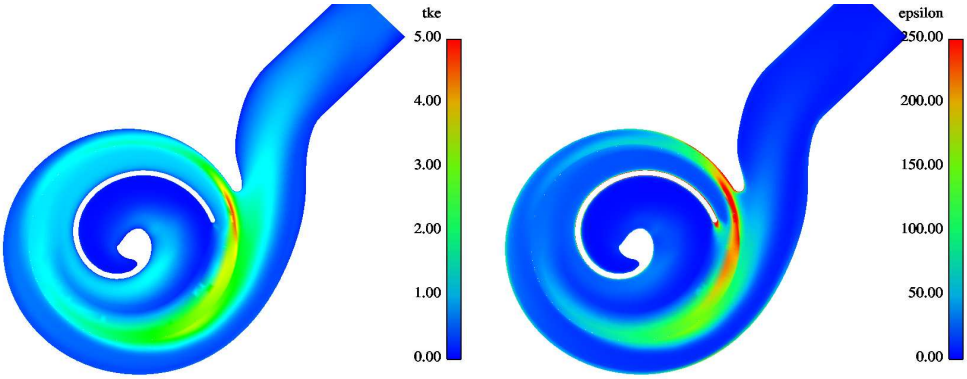

Fig. 24: Distribution of the turbulent kinetic energy (left) and dissipation (right). The plane is the same as in Fig. 23. The mass flow is 16.7 kg/s.

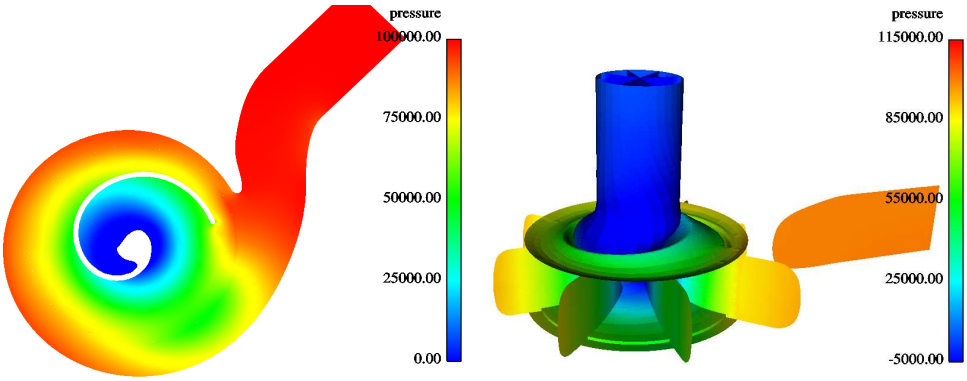

Fig. 25: Pressure distribution at plane 45 mm from the bottom of the impeller (left) and at planes crossing the impeller (right). The mass flow is 16.7 kg/s.

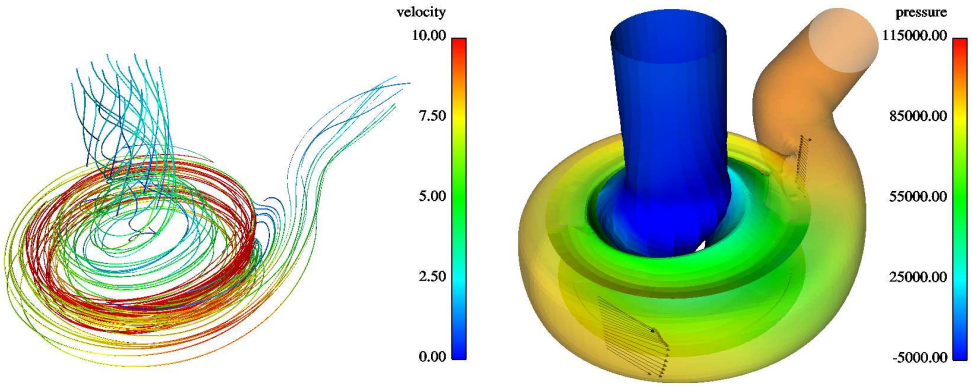

Fig. 26: Streamlines coloured by velocity distribution (left) and velocity vectors at measurement point and pressure distribution at surfaces (right). The mass flow is 16.7 kg/s.

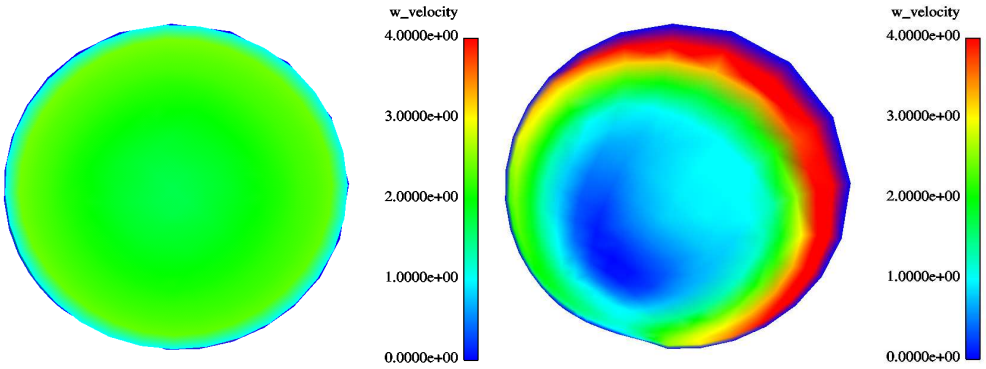

Fig. 27: Velocity distribution at the beginning (left) and at the end (right) of the inlet duct. The mass flow is 16.7 kg/s.

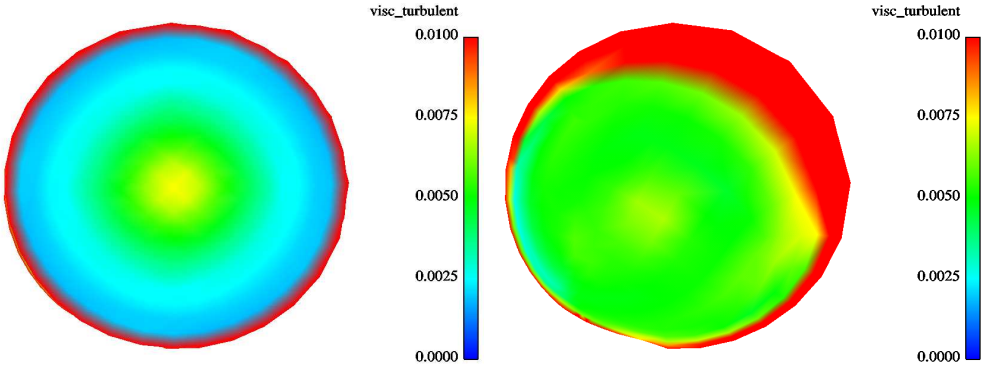

Fig. 28: Distribution of the turbulent viscosity at the beginning (left) and at the end (right) of the inlet duct. The mass flow is 16.7 kg/s.

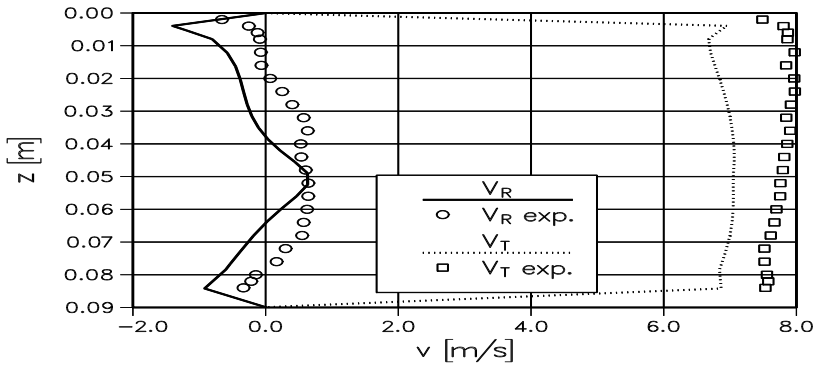

Fig. 29: Velocity distributions at measurement point 1. The mass flow is 16.7 kg/s.

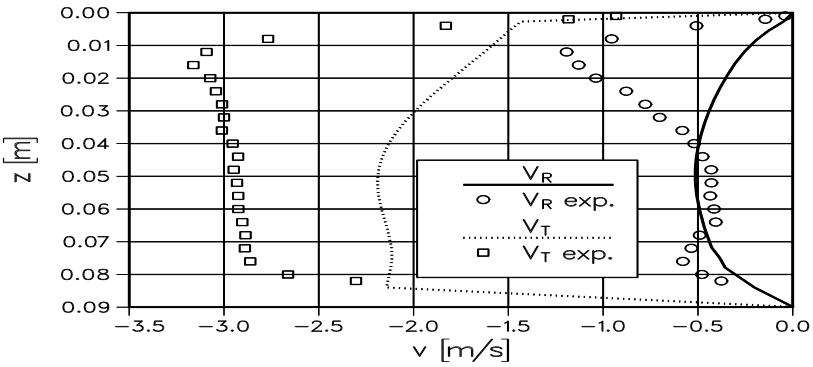

Fig. 30: Velocity distributions at measurement point 2. The mass flow is 16.7 kg/s.

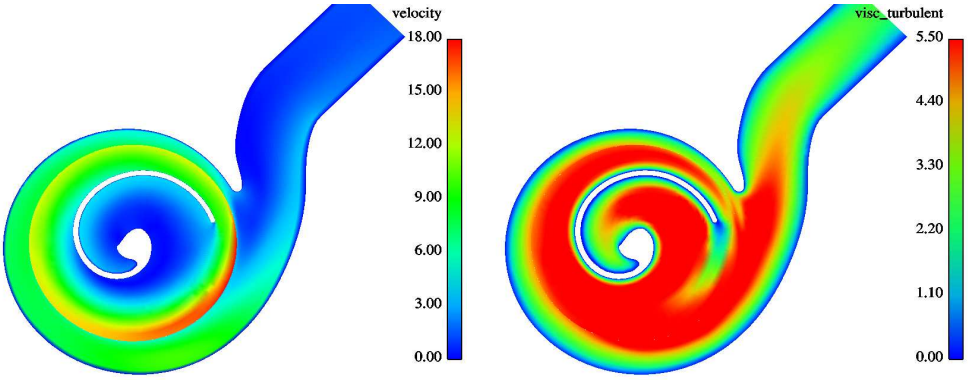

Fig. 31: Velocity distribution at plane 45 mm from the bottom of the impeller (left) and a distribution of the turbulent viscosity at same plane (right). The mass flow is 8.3 kg/s.

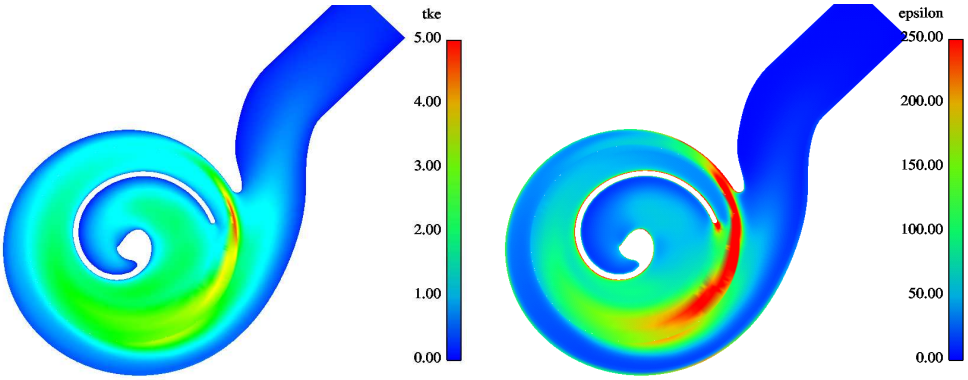

Fig. 32: Distribution of the turbulent kinetic energy (left) and dissipation (right). The plane is the same as in Fig. 31. The mass flow is 8.3 kg/s.

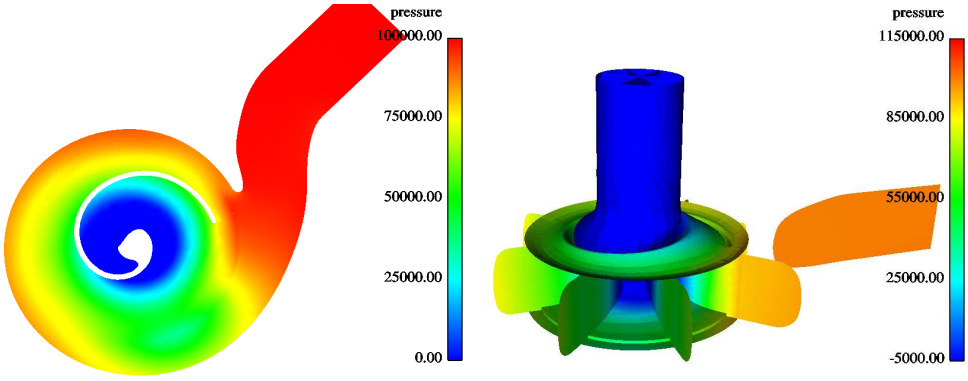

Fig. 33: Pressure distribution at plane 45 mm from the bottom of the impeller (left) and at planes crossing the impeller (right). The mass flow is 8.3 kg/s.

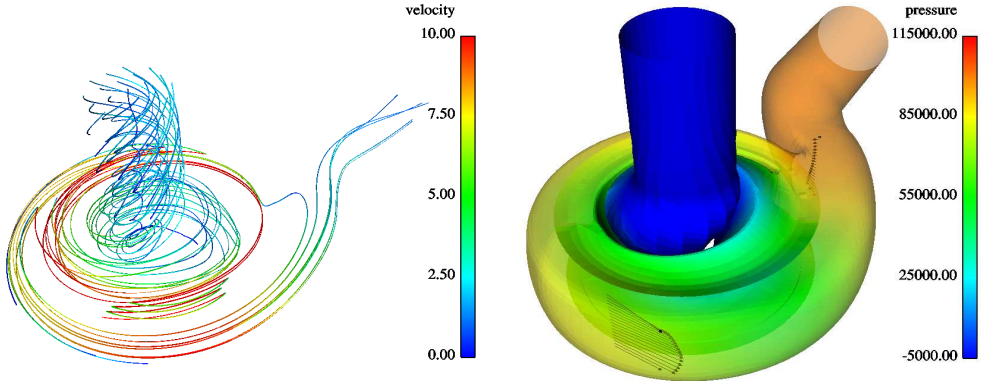

Fig. 34: Streamlines coloured by velocity distribution (left) and velocity vectors at measurement point and pressure distribution at surfaces (right). The mass flow is 8.3 kg/s.

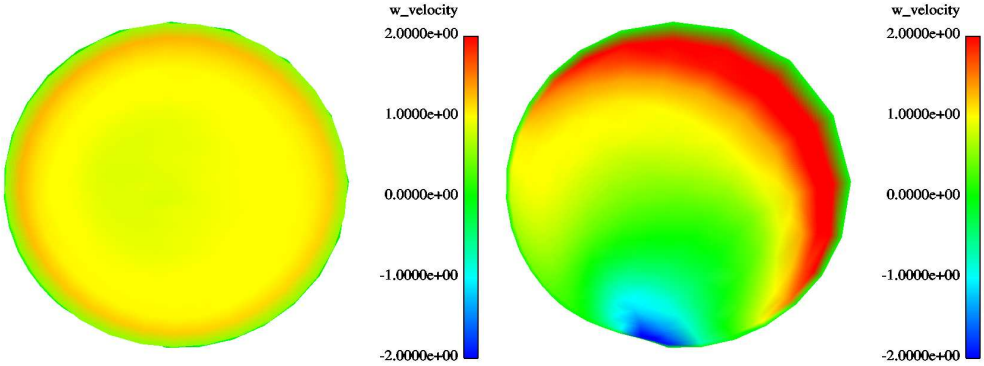

Fig. 35: Velocity distribution at the beginning (left) and at the end (right) of the inlet duct. The massflow is 8.3 kg/s.

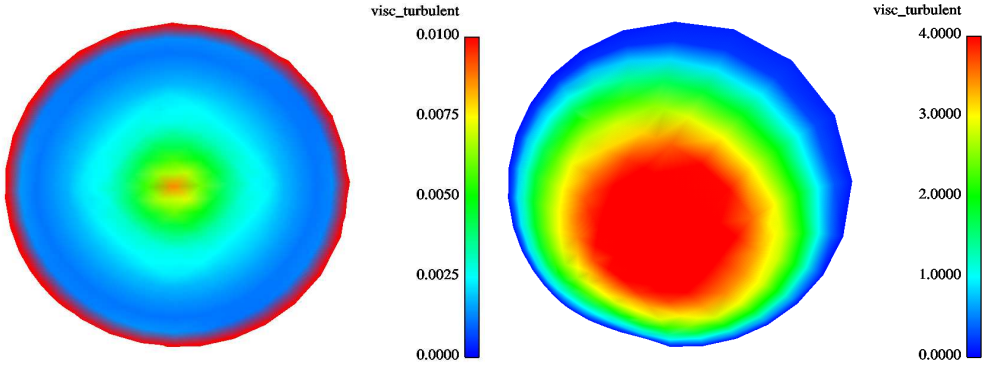

Fig. 36: Distribution of the turbulent viscosity at the beginning (left) and at the end (right) of the inlet duct. The mass flow is 8.3 kg/s.

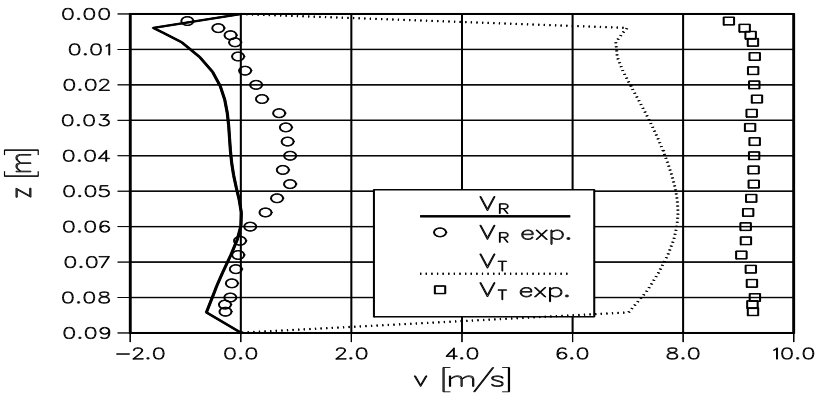

Fig. 37: Velocity distributions at measurement point 1. The mass flow is 8.3 kg/s.

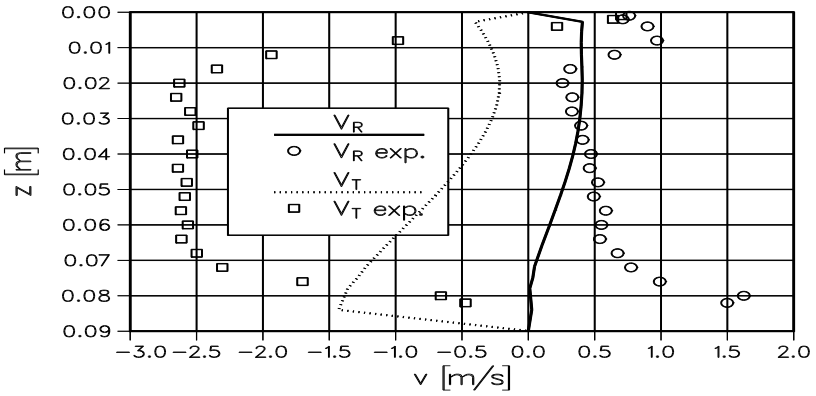

Fig. 38: Velocity distributions at measurement point 2. The mass flow is 8.3 kg/s.

B Distributions of the FINFLO Simulations of the Geometry 2.1 with the Dense Grid

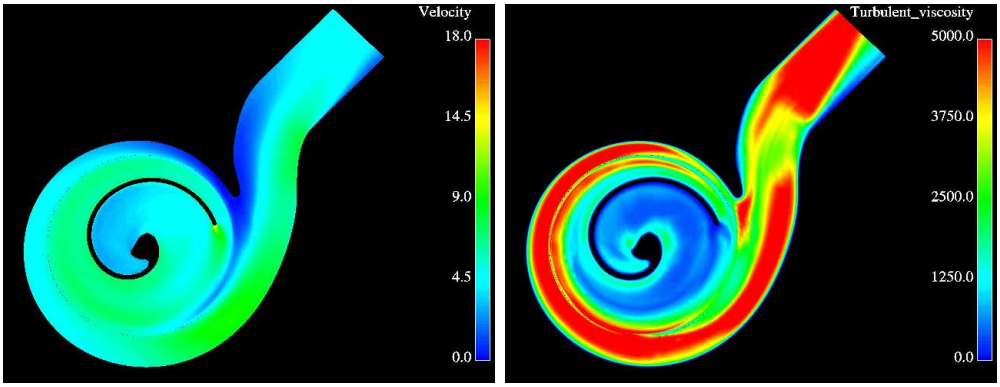

Fig. 39: Velocity distribution at plane 45 mm from the bottom of the impeller (left) and a distribution of the turbulent viscosity at the same plane (right). The mass flow is 30 kg/s.

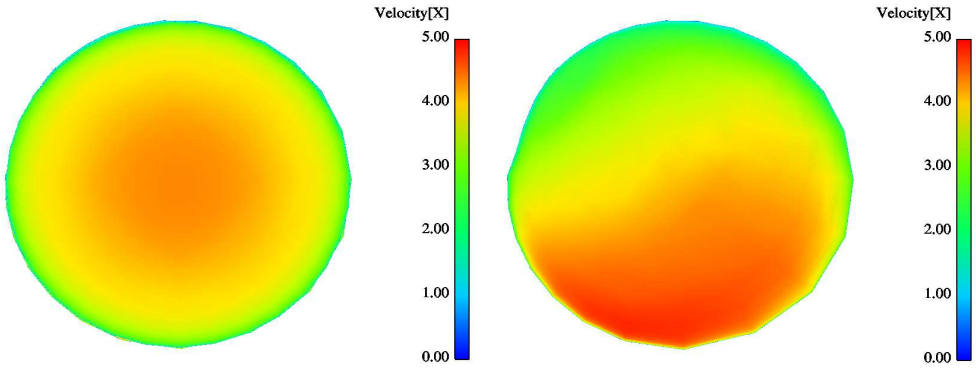

Fig. 40: Velocity distribution at the beginning (left) and at the end (right) of the inlet duct. The mass flow is 30 kg/s.

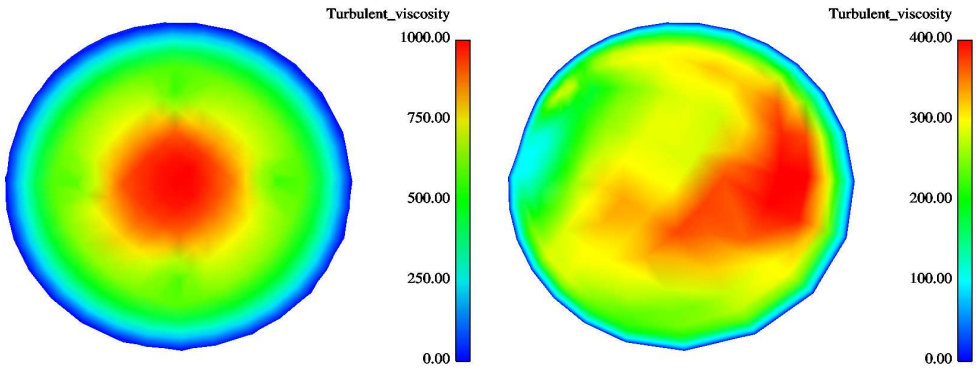

Fig. 41: Distribution of the turbulent viscosity at the beginning (left) and at the end (right) of the inlet duct. The massflow is 30 kg/s.

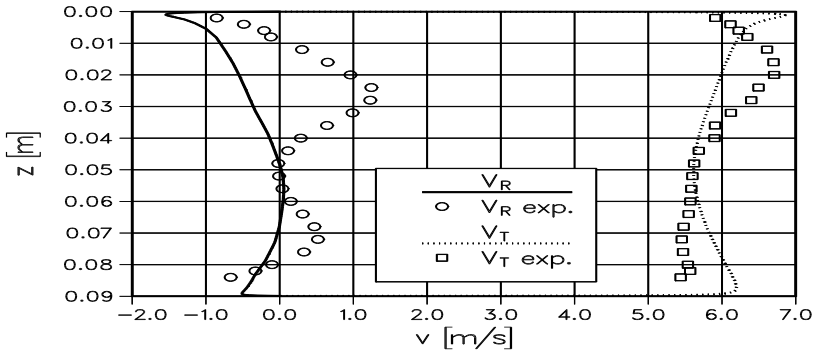

Fig. 42: Velocity distributions at measurement point 1. The mass flow is 30 kg/s.

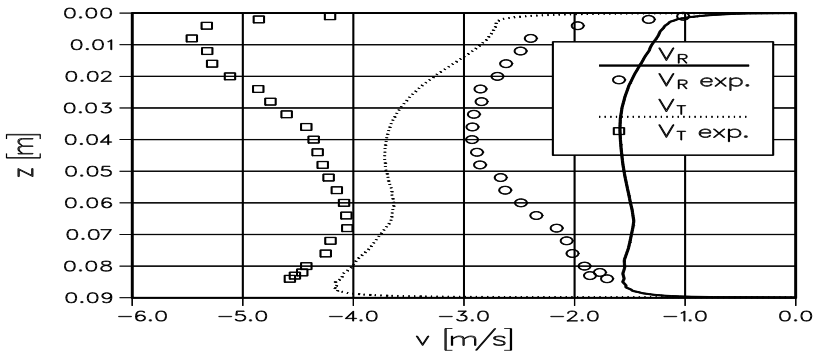

Fig. 43: Velocity distributions at measurement point 2. The mass flow is 30 kg/s.

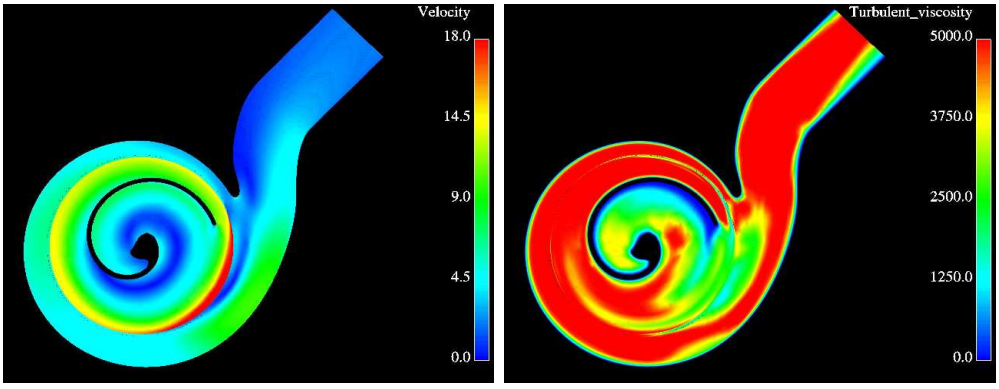

Fig. 44: Velocity distribution at plane 45 mm from the bottom of the impeller (left) and a distribution of the turbulent viscosity at the same plane (right). The mass flow is 15 kg/s.

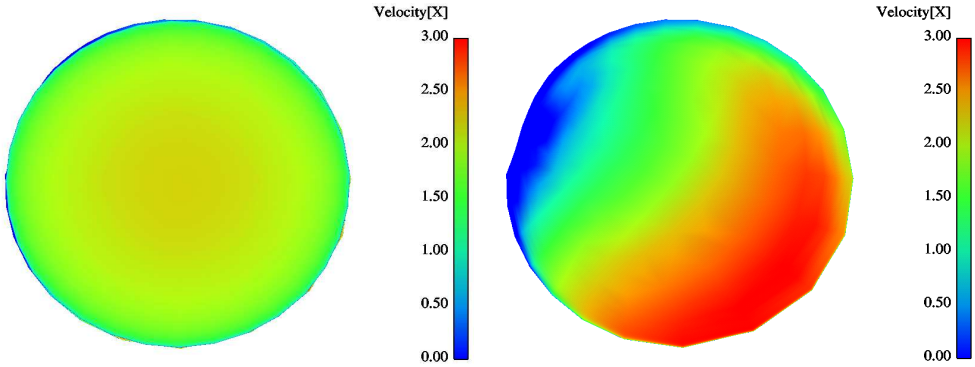

Fig. 45: Velocity distribution at the beginning (left) and at the end (right) of the inlet duct. The mass flow is 15 kg/s.

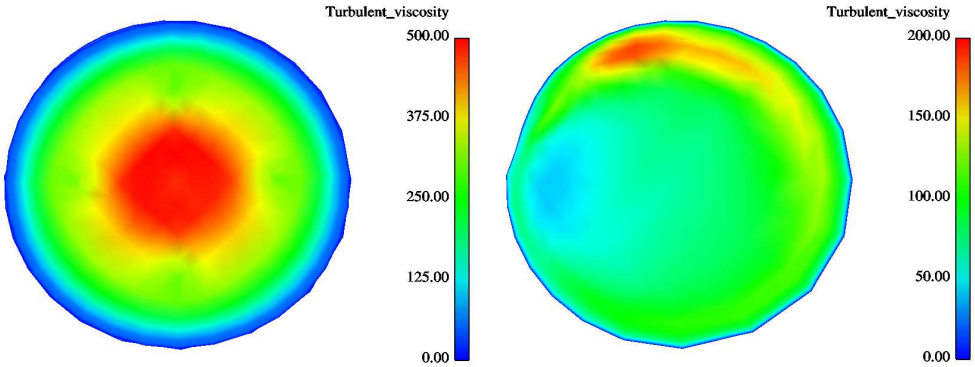

Fig. 46: Distribution of the turbulent viscosity at the beginning (left) and at the end (right) of the inlet duct. The mass flow is 15 kg/s.

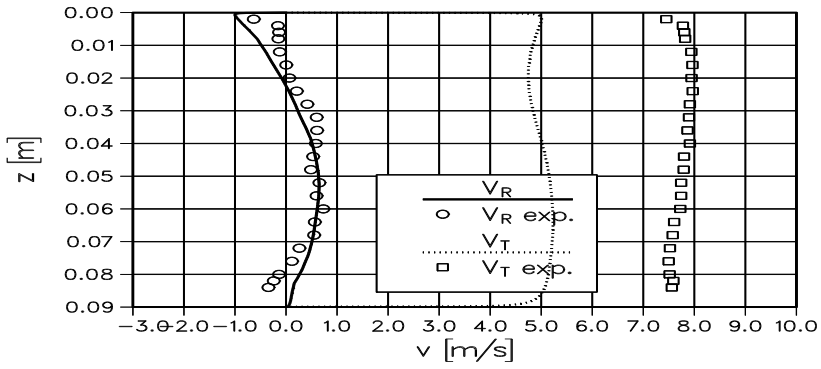

Fig. 47: Velocity distributions at measurement point 1. The mass flow is 15 kg/s.

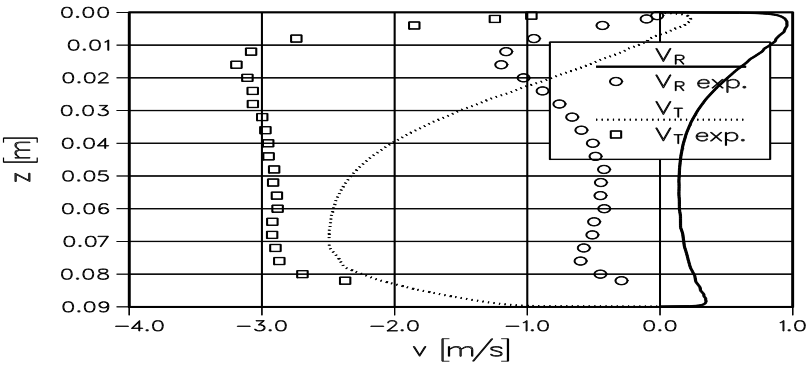

Fig. 48: Velocity distributions at measurement point 2. The mass flow is 15 kg/s.

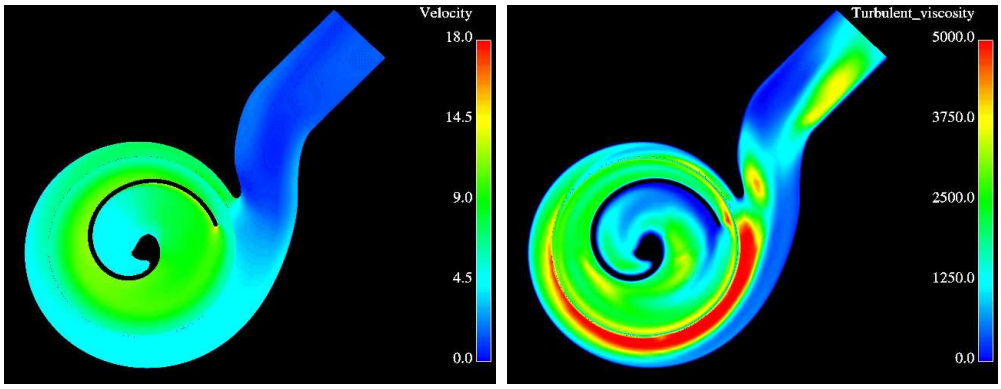

Fig. 49: Velocity distribution at plane 45 mm from the bottom of the impeller (left) and a distribution of the turbulent viscosity at the same plane (right). The massflow is 10 kg/s.

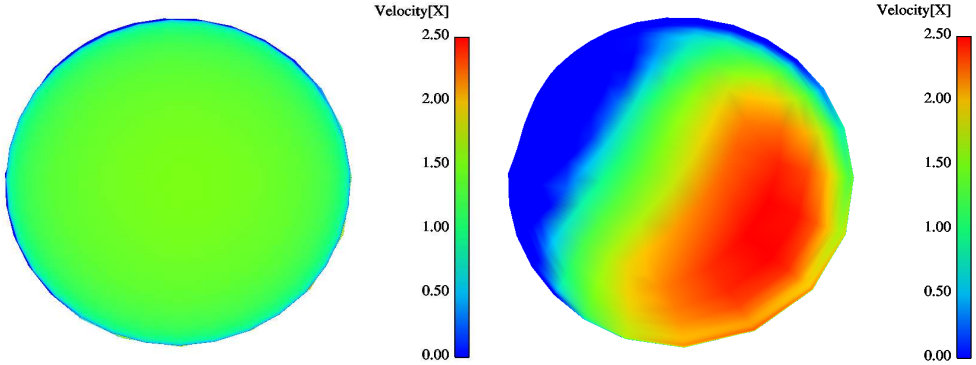

Fig. 50: Velocity distribution at the beginning (left) and at the end (right) of the inlet duct. The mass flow is 10 kg/s.

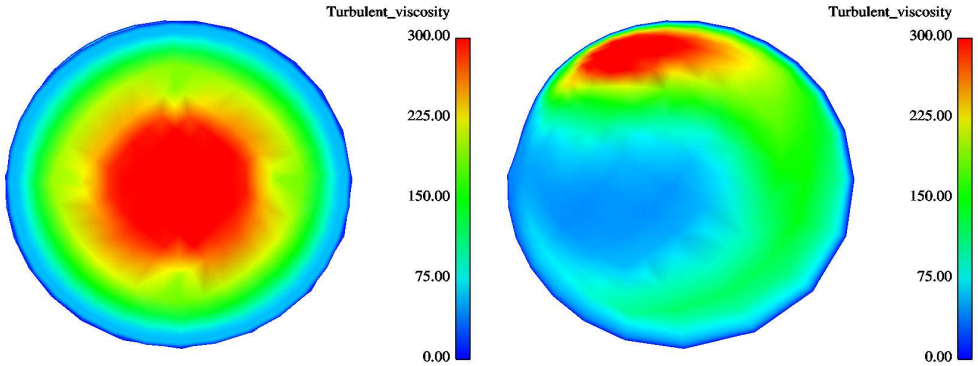

Fig. 51: Distribution of the turbulent viscosity at the beginning (left) and at the end (right) of the inlet duct. The mass flow is 10 kg/s.

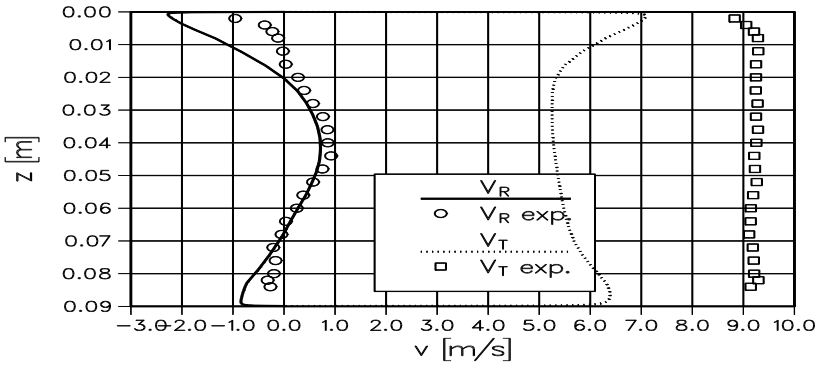

Fig. 52: Velocity distributions at measurement point 1. The mass flow is 10 kg/s.

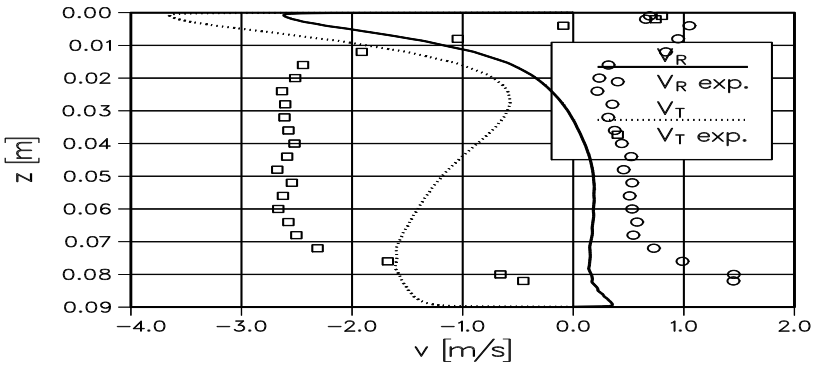

Fig. 53: Velocity distributions at measurement point 2. The mass flow is 10 kg/s.

C Distributions of the Tascflow Simulations of the Geometry 2.2

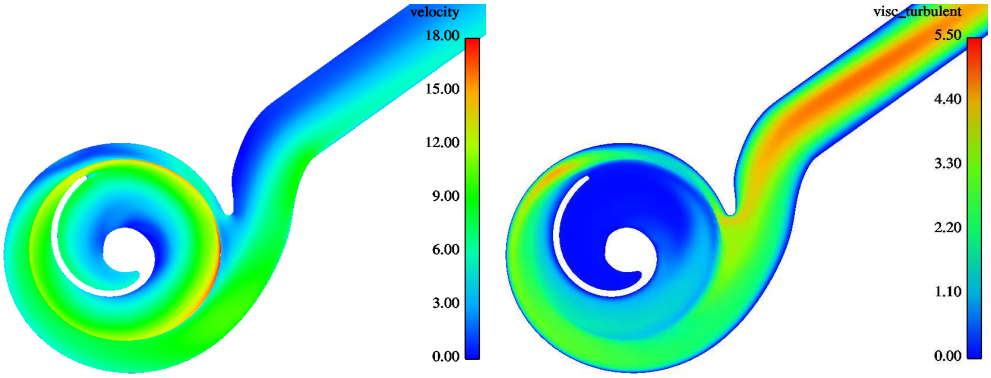

Fig. 54: Velocity distribution at plane 45 mm from the bottom of the impeller (left) and distribution of the turbulent viscosity at same plane (right). The mass flow is 33.3 kg/s.

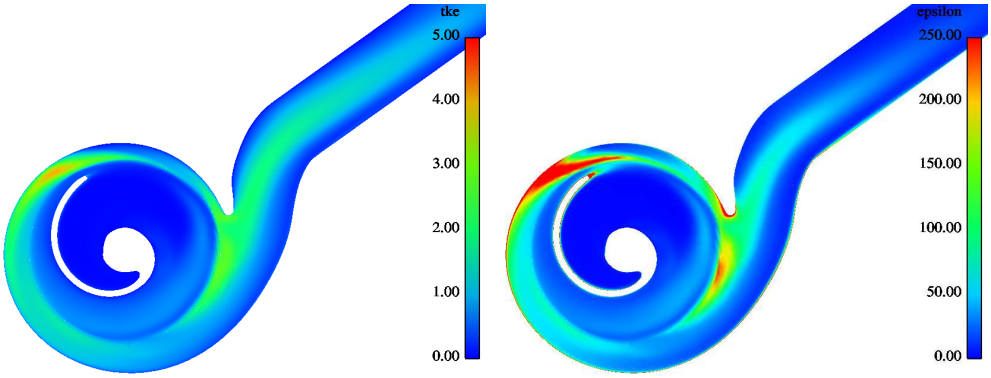

Fig. 55: Distribution of the turbulent kinetic energy (left) and dissipation (right). The plane is the same as in Fig. 54. The mass flow is 33.3 kg/s.

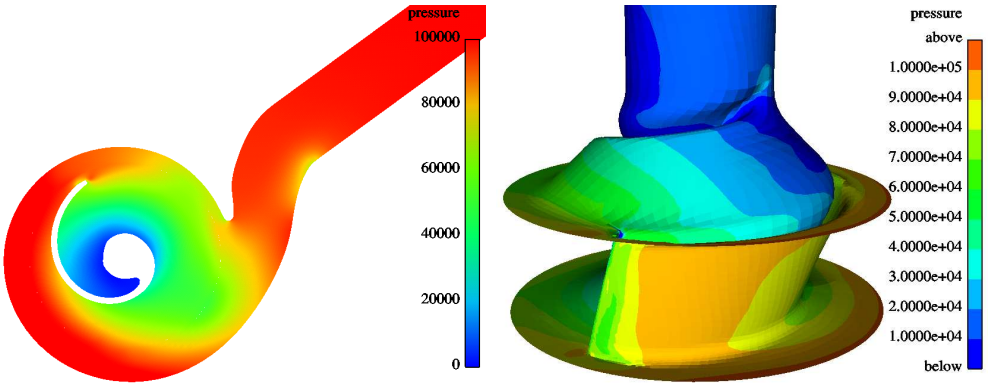

Fig. 56: Pressure distribution at plane 45 mm from the bottom of the impeller (left) and at the impeller surface (right). The mass flow is 33.3 kg/s.

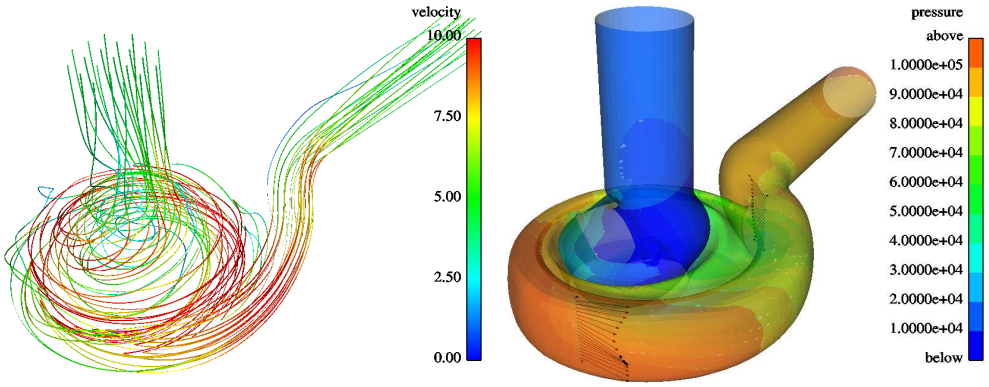

Fig. 57: Streamlines coloured by velocity distribution (left) and velocity vectors at measurement point and pressure distribution at surfaces (right). The mass flow is 33.3 kg/s.

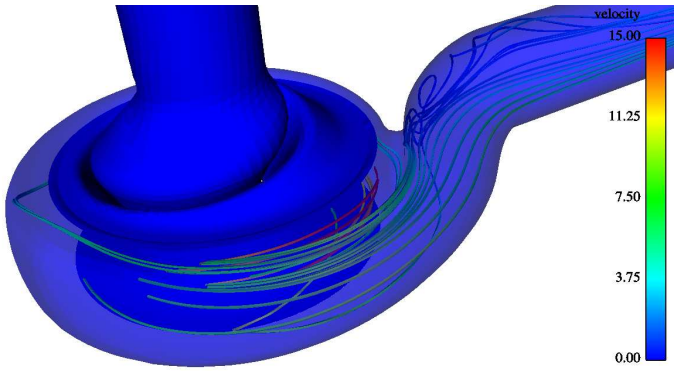

Fig. 58: Streamlines coloured by velocity distribution showing slow velocity area at outlet duct. The mass flow is 33.3 kg/s.

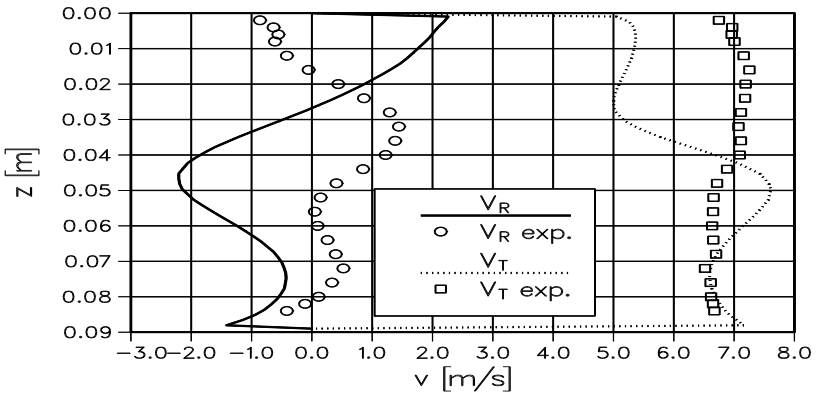

Fig. 59: Velocity distributions at measurement point 1. The mass flow is 33.3 kg/s.

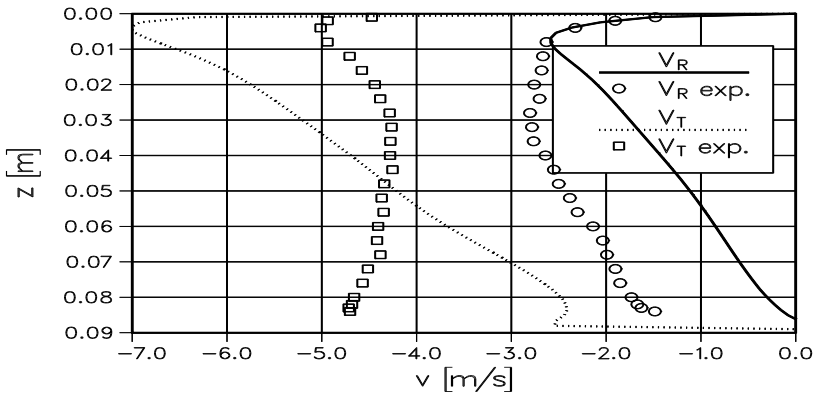

Fig. 60: Velocity distributions at measurement point 2. The mass flow is 33.3 kg/s.

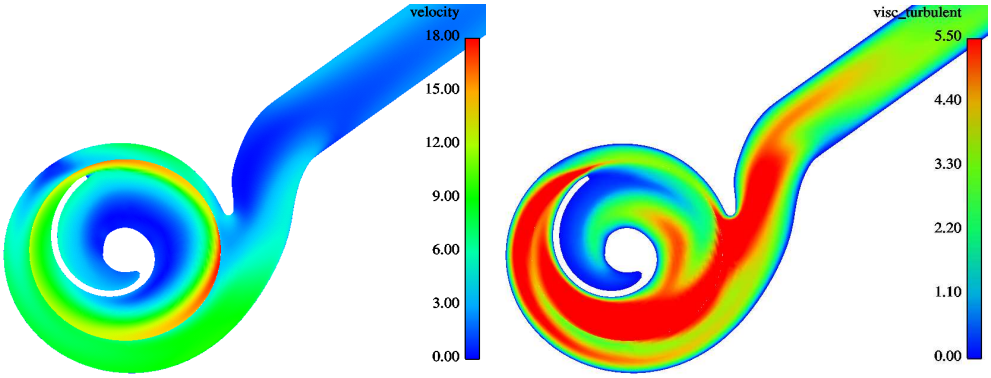

Fig. 61: Velocity distribution at plane 45 mm from the bottom of the impeller (left) and distribution of the turbulent viscosity at same plane (right). The mass flow is 16.7 kg/s.

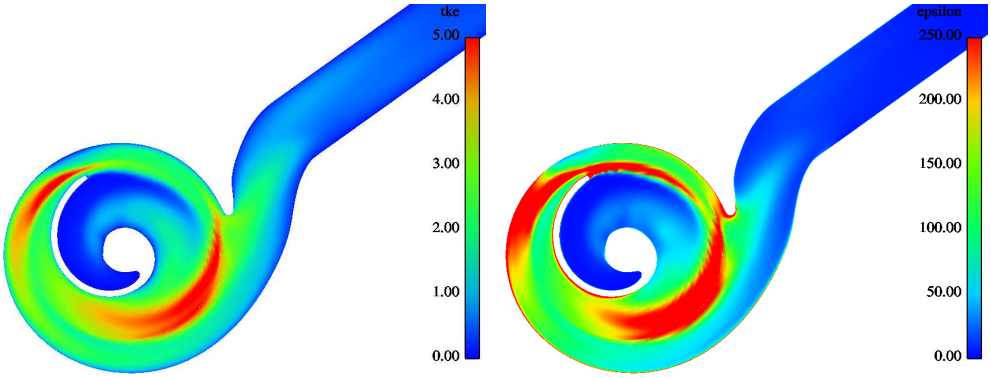

Fig. 62: Distribution of the turbulent kinetic energy (left) and dissipation (right). The plane is the same as in Fig. 54. The mass flow is 16.7 kg/s.

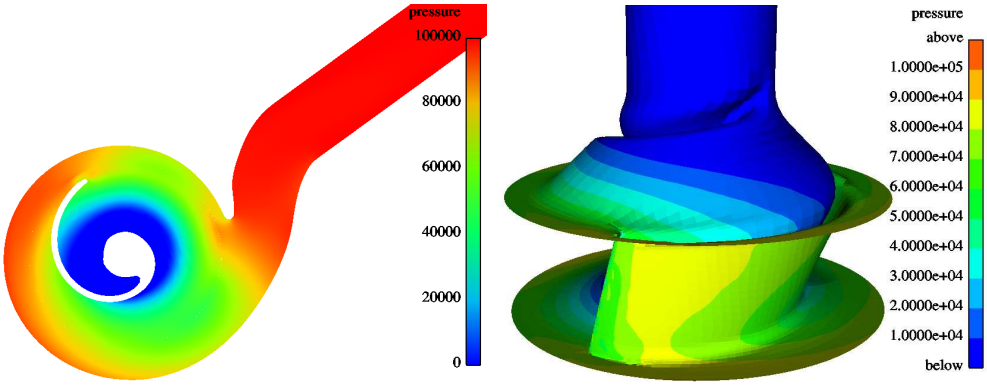

Fig. 63: Pressure istribution at plane 45 mm from the bottom of the impeller (left) and at the impeller surface (right). The mass flow is 16.7 kg/s.

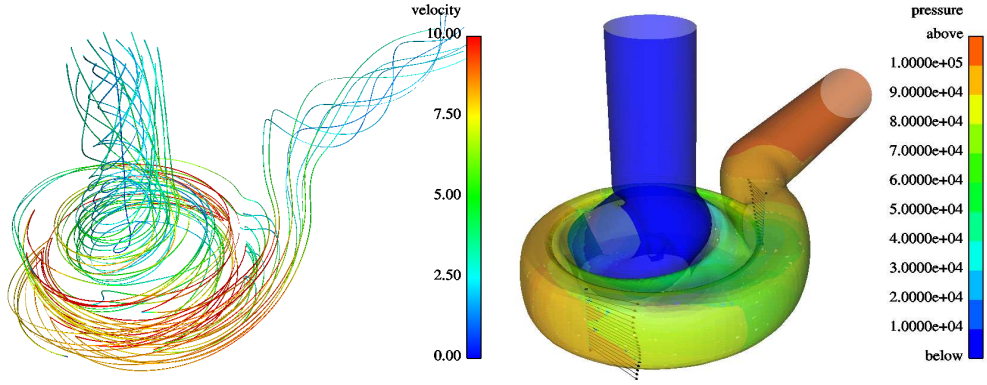

Fig. 64: Streamlines coloured by velocity distribution (left) and velocity vectors at measurement point and pressure distribution at surfaces (right). The mass flow is 16.7 kg/s.

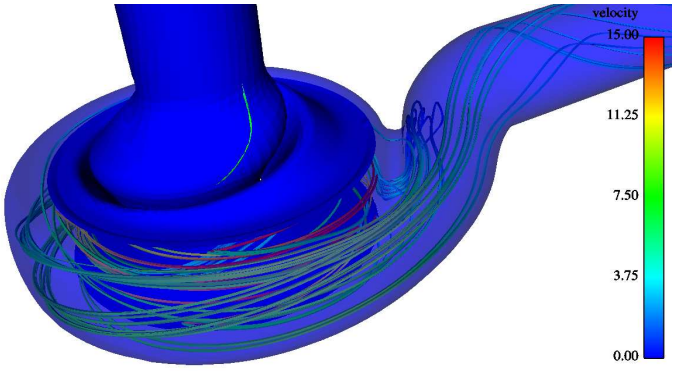

Fig. 65: Streamlines coloured by velocity distribution showing slow velocity area at outlet duct. The mass flow is 16.7 kg/s.

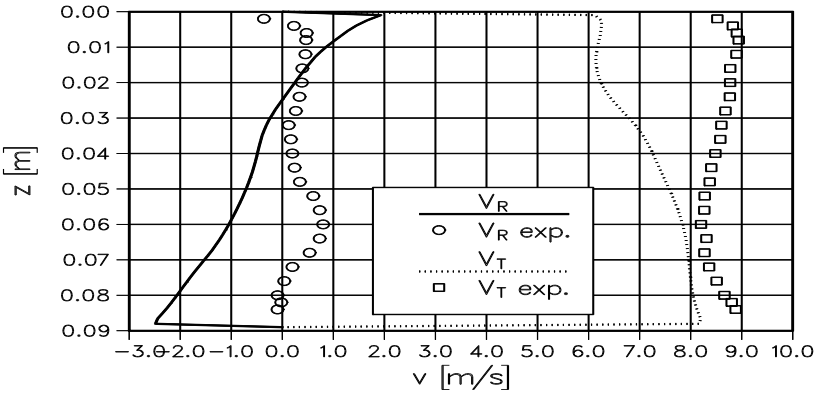

Fig. 66: Velocity distributions at measurement point 1. The mass flow is 16.7 kg/s.

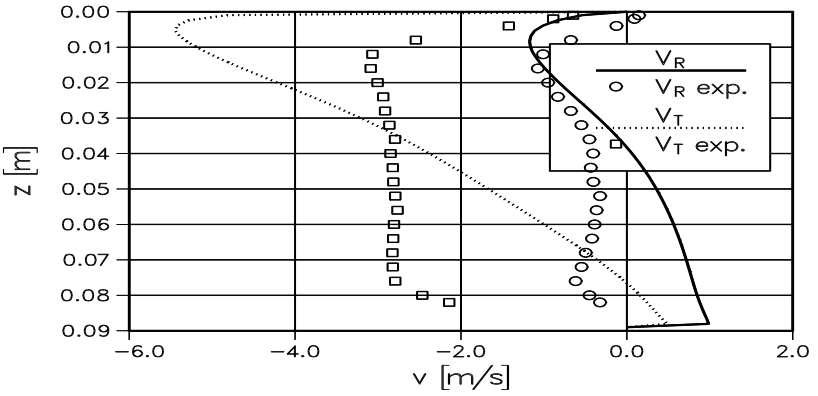

Fig. 67: Velocity distributions at measurement point 2. The mass flow is 16.7 kg/s.